

1N-34
157147

A Computational/Experimental Study of the Flow Around A Body of Revolution at Angle of Attack

Gregory G. Zilliac

September 1986

(NASA-TM-88329) A
COMPUTATIONAL/EXPERIMENTAL STUDY OF THE FLOW
AROUND A BODY OF REVOLUTION AT ANGLE OF
ATTACK (NASA) 34 p

CSCL 200

N90-11254

Unclas
G3/34 0234968

LIBRARY COPY

OCT 10 1986

LANGLEY RESEARCH CENTER
LIBRARY, NASA
HAMPTON, VIRGINIA



National Aeronautics and
Space Administration

A COMPUTATIONAL/EXPERIMENTAL STUDY OF THE FLOW AROUND A BODY OF REVOLUTION AT ANGLE OF ATTACK

Gregory G. Zilliac

SUMMARY

The incompressible Navier-Stokes equations are numerically solved for steady flow around an ogive-cylinder (finesness ratio 4.5) at angle of attack. The three-dimensional vortical flow is investigated with emphasis on the tip and the near-wake region. The implicit, finite-difference computation is performed on the CRAY X-MP computer using the method of pseudocompressibility. Comparisons of computational results with results of a companion towing tank experiment are presented for two symmetric leeside flow cases of moderate angles of attack. The topology of the flow is discussed and conclusions are drawn concerning the growth and stability of the primary vortices.

INTRODUCTION

The motion of a viscous fluid passing by slender body of revolution is an interesting flow to study. The complexity of the vortical flow which can arise belies the simplicity of the body shape. In addition, the fluid-dynamic elements of this flow are common to those found on the components of many flight vehicles.

The nature of the vortex wake structure which develops on a slender body of revolution is primarily dependent on the angle of attack, tip geometry, finesness ratio of the body, and to a lesser degree, Mach and Reynolds number.

On an ogive-cylinder of overall finesness ratio 4.5, (configuration used in the present study) the events that take place as the angle of attack is increased from 0° to 90° can be associated with a sequence of angle of attack regimes (suggested by Allen and Perkins (ref. 1)). At zero angle of attack, the flow is axisymmetric. A small increment in angle of attack produces a crossflow which eventually causes a steady, symmetric longitudinal vortex pair to form on the leeside of the body when the angle of attack exceeds a certain minimum. The strength of these vortices, called primary vortices, continues to increase with increasing angle of attack. Evidence of the formation of secondary vortices of opposite sense to the primary vortices may be found near the surface of the ogive. At a critical angle of attack of approximately 35° , an asymmetric disturbance somewhere in the flow causes a dramatic change in the orientation of the primary vortices to a new stable, asymmetric state. For angles of attack greater than 60° , the flow becomes unsteady and as the angle of attack approaches 90° a vortex street forms in a manner similar to that found for a two-dimensional circular cylinder.

Side forces approaching the magnitude of the normal force have been attributed to the highly asymmetric vortex orientations on the leeside of the body. On bodies of greater finesness ratio, an array of up to eleven vortices alternating in sign have been observed. The process by which these additional primary vortices form involves the formation, growth

and shedding of the secondary vortices along the length of the body. The mechanisms which cause the flow to become asymmetric are not currently understood. Several hypotheses have been formulated based on the impulsive flow analogy which relates the three-dimensional steady flow past a pointed slender body to the two-dimensional unsteady flow around a circular cylinder. So far, the analogy has not been fully proven.

The objectives of this paper are to demonstrate that a valid computation of the symmetric flow around an ogive-cylinder at angle of attack can be achieved in the laminar flow regime, and secondly, to provide further insight into the mechanisms which govern the growth and stability of the leeside vortical structure. The ultimate goal of this research program is to investigate the asymmetric, turbulent flow on bodies of revolution at angle of attack and at moderate Reynolds number using a combined computational/experimental approach. Successful treatment of the low-Reynolds-number symmetric flows considered in this report is intended to be a stepping-stone to these more ambitious attempts.

METHOD OF SOLUTION

Governing Equations

The flow around a slender body of revolution at moderate to high angles of attack and low Mach number is a complicated vortical flow with viscous effects playing a primary role in the development of the vortical structure. As a consequence, the solution of the incompressible Navier-Stokes equations is required. Flow visualization studies reveal that the flow about the ogive is steady for angles of attack less than 60° ; thus, a time-accurate computation is not necessary. For sufficiently low Reynolds number, the flow around the ogive is laminar. In a curvilinear coordinate system, the Navier-Stokes equations in mass-averaged variables (including the pseudocompressibility terms) can be written in the following form:

$$\frac{\partial p}{\partial t} + \beta \left(\frac{\partial u}{\partial x} + \frac{\partial v}{\partial y} + \frac{\partial w}{\partial z} \right) = 0 \quad (1)$$

$$\frac{\partial \hat{D}}{\partial \tau} + \frac{\partial}{\partial \xi} (\hat{E} - \hat{E}_v) + \frac{\partial}{\partial \eta} (\hat{F} - \hat{F}_v) + \frac{\partial}{\partial \zeta} (\hat{G} - \hat{G}_v) = 0$$

where

$$\hat{D} = \frac{1}{J} \begin{bmatrix} p \\ u \\ v \\ w \end{bmatrix}, \hat{E} = \frac{1}{J} \begin{bmatrix} \beta U + \xi_t(p - \beta) \\ uU + \xi_x p \\ vU + \xi_y p \\ wU + \xi_z p \end{bmatrix}, \hat{F} = \frac{1}{J} \begin{bmatrix} \beta V + \eta_t(p - \beta) \\ uV + \eta_x p \\ vV + \eta_y p \\ wV + \eta_z p \end{bmatrix}, \hat{G} = \frac{1}{J} \begin{bmatrix} \beta W + \zeta_t(p - \beta) \\ uW + \zeta_x p \\ vW + \zeta_y p \\ wW + \zeta_z p \end{bmatrix},$$

$$\hat{E}_v = \begin{bmatrix} 0 \\ \tau_{xx} \\ \tau_{xy} \\ \tau_{xz} \end{bmatrix}, \hat{F}_v = \begin{bmatrix} 0 \\ \tau_{yx} \\ \tau_{yy} \\ \tau_{yz} \end{bmatrix}, \hat{G}_v = \begin{bmatrix} 0 \\ \tau_{zx} \\ \tau_{zy} \\ \tau_{zz} \end{bmatrix} \quad (2)$$

The transformation used is of the form

$$\begin{aligned} \tau &= t \\ \xi &= \xi(x, y, z, t) \\ \eta &= \eta(x, y, z, t) \\ \varsigma &= \varsigma(x, y, z, t) \end{aligned} \quad (3)$$

with the Jacobian defined as

$$J = \begin{bmatrix} \xi_x & \xi_y & \xi_z \\ \eta_x & \eta_y & \eta_z \\ \varsigma_x & \varsigma_y & \varsigma_z \end{bmatrix} \quad (4)$$

and the contravariant velocities

$$\begin{aligned} U &= \xi_t + \xi_x u + \xi_y v + \xi_z w \\ V &= \eta_t + \eta_x u + \eta_y v + \eta_z w \\ W &= \varsigma_t + \varsigma_x u + \varsigma_y v + \varsigma_z w \end{aligned} \quad (5)$$

For an orthogonal grid, the viscous flux terms are defined by

$$\begin{aligned} \hat{E}_v &= \frac{\nu}{J} (\xi_x^2 + \xi_y^2 + \xi_z^2) Im \frac{\partial D}{\partial \xi} + (R_{xx} \dots terms) \\ \hat{F}_v &= \frac{\nu}{J} (\eta_x^2 + \eta_y^2 + \eta_z^2) Im \frac{\partial D}{\partial \eta} + (R_{yx} \dots terms) \\ \hat{G}_v &= \frac{\nu}{J} (\varsigma_x^2 + \varsigma_y^2 + \varsigma_z^2) Im \frac{\partial D}{\partial \varsigma} + (R_{zx} \dots terms) \end{aligned} \quad (6)$$

where

$$D = [p, u, v, w]^T$$

and

$$Im = \begin{bmatrix} 0 & 0 & 0 & 0 \\ 0 & 1 & 0 & 0 \\ 0 & 0 & 1 & 0 \\ 0 & 0 & 0 & 1 \end{bmatrix} \quad (7)$$

In the above equations, β is a pseudocompressibility parameter which alters the character of the finite-differenced equations to one of a hyperbolic form. This character change allows the use of an implicit scheme and relaxes the strict incompressibility requirement during the convergence process. Upon reaching steady state, the effect of β on the solution is negligible. Hence, the steady solution that is obtained is essentially a solution of the incompressible Navier-Stokes equations.

In this investigation the INS3D computer code developed by Kwak, Chang, Shanks, and Chakravarthy (ref. 2) is applied to solve the equations for flow around an ogive-cylinder body. The numerical approach used in the INS3D computer code is described in great detail in reference 2. Briefly, the governing equations including the pseudocompressibility terms are written in finite-difference form using central differences for the spatial terms. These equations are approximately factored using the factorization technique of Beam and Warming (ref. 3). Implicit second-order and explicit fourth-order numerical dissipation is added to damp out high-frequency oscillations. The solution is advanced in time until a steady state is reached.

The configuration of the ogive-cylinder model is similar to, and in certain cases, identical to configurations used in past experimental studies (ref. 4). The body is a tangent ogive-cylinder of fineness ratio 3.5 with a cylindrical afterbody of fineness ratio 1. The ξ, η, ζ curvilinear coordinate system corresponds to the normal, axial, and tangential transformed coordinates of the ogive. The tip of the ogive is the location of the origin of the (x, y, z) physical coordinates.

In order to accurately capture the variety of length scales of the flow careful attention must be paid to the computational mesh. Near the tip of the ogive, a region of high gradients exists owing to the presence of a stagnation point and in addition, because the tip is the origin of the leeside vortices. Experiments (ref. 5) have demonstrated that very small changes in the tip geometry can have a dramatic effect on the orientation of the leeside vortices. In this study, points were clustered at the tip and rear of the afterbody using a cosine point distribution. A two-dimensional poisson grid generator (GRAPE, ref. 6) was used to distribute the mesh points in a plane passing through the body axis of symmetry. This plane was then rotated about the body axis of symmetry to form a three-dimensional wrapped mesh. The grid outer boundary is spherical, and is located 6 body lengths from the tip of the ogive. This wrapped grid approach was chosen over three-dimensional grid generation schemes to ensure grid symmetry and also orthogonality. A minor drawback of the wrapped grid approach is that the axis around which the grid is wrapped becomes a numerical singular line. On this line a one-to-one correspondence between the physical and computational domains no longer exists. To maintain stability and accuracy, no grid points were placed on this axis. Figure 1 shows the mesh which was

used for this study. The grid is comprised of 49 by 39 by 68 points in the normal, axial, and tangential directions, respectively.

Near the surface of the ogive, the mesh spacing was chosen to resolve the viscous effects present in the boundary layers. After extensive study of the effects of grid spacing on accuracy, a minimum of seven grid points were placed in the attached boundary layer normal to the surface to capture the large gradients present.

There are several possible sources of error in the numerical method which may affect the accuracy of the solution. These errors include the effects of the second- and fourth-order artificial viscosity, truncation error, numerical bias, nonresolution of subgrid length scales, and boundary condition errors. The effects of the artificial viscosity and truncation errors are discussed in references 7 and 8. These effects were shown by analysis and example to be minimal, provided that the level of explicit artificial viscosity acting on the pressure is allowed to decay during the solution process. To test the resolving capability of the mesh, the number of gridpoints was cut in half, and the impact on the solution was observed. The effect was found to be minor. The bias errors are thought to be minimal owing to the high degree of symmetry in the solution. Estimates of the effects of boundary condition errors are difficult to quantify and are a continuing area of research.

Boundary and Initial Conditions

Boundary conditions must be prescribed on the six faces of the computational cube, and in addition, these conditions must be well-posed and lead to a stable numerical solution. The numerical boundary conditions consist of specifying conditions on the pressure and velocities on the body surface, at the inflow and outflow boundaries, and near the grid axis of revolution. In addition to these four boundary conditions, a circumferential periodicity condition is imposed. These conditions, which do not enforce symmetry of the solution, are explained in greater detail below.

Body Surface:

$$u = v = w = 0, \quad \frac{\partial p}{\partial \xi} = 0 \quad (8)$$

Inflow:

$$u = U_{\infty} \cos \alpha, \quad v = 0, \quad w = U_{\infty} \sin \alpha, \quad p = p_{\infty} \quad (9)$$

Outflow:

$$q^{n+1}(\xi_{max}, \eta, \zeta) = \{q(\xi_{max-1}, \eta, \zeta) + R[q(\xi_{max}, \eta, \zeta) - q(\xi_{max-2}, \eta, \zeta)]\}^n \quad (10)$$

where q is the vector of dependent variables p , u , v , and w , and R is the extrapolation weight factor.

The extrapolated outflow pressure is additionally modified by the parameter S . This parameter is determined by solving a simplified momentum equation and is required to insure that mass and momentum are conserved during the extrapolation of the outflow velocities. The reader is referred to reference 7 for a deeper explanation of this procedure.

$$p^{n+1}(\xi_{max}, \eta, \zeta) = S [\hat{p}^{n+1}(\xi_{max}, \eta, \zeta)] \quad (11)$$

where

$$S = \frac{\int_{exit} (\text{momentum corrected pressure}) d\hat{a}}{\int_{exit} (\text{extrapolated pressure}) d\hat{a}} \quad (12)$$

Near the grid axis of revolution:

$$q^{n+1}(\xi, \eta, \zeta_{max}) = \{q(\xi, \eta, \zeta_{max-1}) + R[q(\xi, \eta, \zeta_{max}) - q(\xi, \eta, \zeta_{max-2})]\}^n \quad (13)$$

Initial Conditions:

$$q^0(\xi, \eta, \zeta) = 1.0 \quad (14)$$

At the beginning of the convergence process, the dependent variables are initialized to 1.0 in the interior of the computational domain.

TOWING TANK STUDY

A companion towing tank study was performed in a 55 gallon tank apparatus (fig. 2) using a 4-in. long aluminum ogive-cylinder model. The Reynolds number and model configuration are identical to those in the computation aside from a small sting which was used to support the model. Flow in the crossflow plane was visualized by taking a time exposure of the induced motion of a saltwater suspension of neutrally buoyant pliolite particles (approximate diam of 0.0035 in.). To improve the laser sheet crossflow plane visualization, a cylindrical lens in combination with a short focal-length lens was used to produce a 3/10-in.-thick laser light sheet. The model was moved through the water by a traversing mechanism and short time-exposure photographs of the induced particle motion were taken.

The particle streaks recorded on the photographs correspond to crossflow instantaneous streamline patterns. The camera and laser sheet were moved with the model to produce the instantaneous streamline pattern as would be seen by an observer in the model's frame of reference. After transient effects introduced at the startup of the motion

have diminished and the flow has reached steady state, the particle streaks indicate the steady streamline pattern. Information concerning the velocity direction and magnitude can be obtained from the image by measuring the length and orientation of the particle streaks.

NUMERICAL AND EXPERIMENTAL RESULTS

Analysis of three-dimensional results is a complicated task owing to the inherent difficulties associated with presenting and understanding physical quantities which vary in three spatial directions. Two different approaches to presenting the data are used in this section to cope with the difficulties. In the first approach, data are presented in two-dimensional crossflow planes at different locations along the body. Although this approach has limitations, it is very useful for a flow that is conical or where the flow in the third dimension is slowly evolving. The second approach involves the three-dimensional display of data such as particle path lines. Three dimensional displays of data can sometimes be deceptive owing to perspective difficulties, but these displays overcome the limitation of the first approach. In the following discussion, some common topological terms (saddle, node, etc...) are used to describe the flow in the crossflow plane as has been the practice for some time (ref. 9).

The two cases computed were for an $L/D = 3.5$ ogive with a cylindrical afterbody of $L/D = 1.0$ at angles of attack of 30° and 45° . The Reynolds number was 1000, based on the freestream velocity and overall body length. A comparison of the computed crossflow velocity vectors with the corresponding instantaneous streamlines obtained from the towing-tank study is presented in figure 3 (a-e) for $\alpha = 30^\circ$ and in figure 4 (a-e) for $\alpha = 45^\circ$ (\tilde{y} and \tilde{z} denote crossflow-plane coordinates). These figures show the development of the flow in crossflow planes at different axial stations along the body. In general, the flow development is similar for the two angles of attack. In both cases, the vortices assume a symmetric orientation. At $X/L = 0.2$ (figs. 3a, 4a) no recirculating flow region is present. At this station the flow resembles the initial flow observed on an impulsively started, two-dimensional circular cylinder. The second station at $X/L = 0.4$ (figs. 3b, 4b) shows the beginning signs of a recirculation zone, and for the $\alpha = 45^\circ$ case (fig. 4b), evidence of a saddle point has appeared on the leeward axis of symmetry. A closeup view of this flow is shown in figure 5. In addition to the saddle point on the leeward side, the flow on the windward side of the body shows a zero azimuthal velocity point, development of the crossflow boundary layer to either side of this point, and acceleration of the crossflow as it passes around the body. The third frame ($X/L = 0.6$) of the $\alpha = 30^\circ$ (fig. 3c) case shows distinctive crossflow separation points, but there is still no evidence of the leeward saddle formation for this case. At $X/L = 0.8$ (figs. 3d, 4d) the flow shows distinctive separation points, saddle points and vortex core centers for both cases. The final frames ($X/L = 0.95$) (figs. 3e, 4e), vividly show the primary vortices in their near fully developed state. In addition, the crossflow separation points on the surface have moved in the windward direction creating pockets of nearly stagnant fluid near these points, but no evidence of secondary vortices is present in either the experimental or the computational results.

In general terms, the sequence of events which occurs during the development of the vortex flowfields is the same for the two cases studied. The primary difference between the cases is the rate at which the vortices develop along the length of the ogive. This result is consistent with the impulsive flow analogy which suggests that it should take a longer axial distance for the primary vortices to develop on the same body at lower angles of attack.

The symmetry plane flow ($y = 0$) over the aft portion of the ogive-cylinder is shown in figure 6 for the $\alpha = 30^\circ$ case. Accuracy of this base-flow result may be influenced by a small degree of unsteadiness which is not captured by INS3D, but for completeness, this result has been included. As expected, a region of low velocity forms immediately to the rear of the cylinder. Fluid originating on the leeside is drawn into this low velocity region and is turned towards the streamwise direction by the high velocity fluid which separates from the windward side of the cylinder.

Computed surface pressure plots are shown in figures 7 and 8 for the two cases investigated. Considering the $\alpha = 45^\circ$ case (fig. 8), one can deduce several interesting features about the vortical flow from the crossflow pressure distribution. As expected, at each value of X/L the maximum pressure point is located on the windward ray ($\theta = 0^\circ$). The maxima decrease in magnitude progressively from the tip to the end of the body along the windward ray. Near the tip of the ogive ($X/L = 0.2$), the circumferential pressure variation is the largest of the five stations considered, and the circumferential pressure gradient remains favorable until approximately $\theta = 115^\circ$. At $X/L = 0.95$, the circumferential pressure variation is the smallest and the onset of adverse pressure gradient occurs at approximately $\theta = 80^\circ$. The behavior of the pressure at the intermediate stations falls between these two extremes. These same trends apply to the $\alpha = 30^\circ$ case (fig. 7) and are the expected trends based on the impulsive flow analogy.

Vorticity contours of the flow field provide further insight into the way in which the flow is determined. The axial vorticity contours (ω_x) for the two cases computed (at $X/L = 0.2$ and $X/L = 0.95$), are presented in figures 9 (a,b) and 10 (a,b). The intermediate stations have the same basic character of these two planes. At the windward ray, the vorticity is a minimum and then progressively increases to a maximum and then decreases back to zero at the leeward ray. The vorticity maxima are located at approximately 45° on either side of the windward ray. These vorticity plots are very reminiscent of typical two-dimensional cylinder vorticity contours.

Three-dimensional representations of the flow field are presented in figures 11 and 12. Particles were released from points in the windward boundary layer at several axial positions. The particles then pass around the body, are entrained into the leeside vortical flow, and then they continue downstream. The differences between the two cases are most evident in these particle path lines. The vortical flow appears to be stronger for the $\alpha = 45^\circ$ (fig. 12) case and also, the vortical flow develops over a shorter distance.

The corresponding surface skin-friction lines are presented in figures 13 and 14. These skin friction lines are the computational analog to surface oil-flow visualizations and were produced by releasing particles on the surface and then by following their trajectories. Blue particles were released near the windward ray and red particles were released on the leeward ray. Magenta particles were used to define ambiguous areas. The red and blue particles flow towards each other and form a line where the azimuthal component of the

skin friction is zero. This line, which does not emanate from a saddle point, (unlike a global line of separation) is a characteristic of what has previously been referred to as "open separation" and also "local separation". These results are similar to the oil-flow results presented in recent studies of pointed bodies of revolution (ref. 4).

CONCLUSIONS

The flow over a pointed body of revolution has been studied from an experimental and computational viewpoint. Comparisons of computational results based on the Navier-Stokes equations and flow visualization results are favorable and tend to validate the accuracy of the computation in a qualitative manner. Analysis of the development of the symmetric vortical flow-field reaffirms the utility of the impulsive flow analogy in understanding the qualitative nature of the flow.

REFERENCES

1. Allen, H.J.; and Perkins, E.W.: Characteristics of Flow Over Inclined Bodies of Revolution, NACA RM-A50L07, 1951.
2. Kwak, D.; and Chang, J.L.C.; and Shanks, S.P.: An Incompressible Navier-Stokes Flow Solver in Three-Dimensional Curvilinear Coordinate System Using Primitive Variables, AIAA paper 84-0253, Jan. 1984.
3. Beam, R.M.; and Warming, R.F.: An Implicit Finite-Difference Algorithm for Hyperbolic Systems in Conservation Law Form, *Journal of Computational Physics* vol. 22, Sept. 1976., pp. 87-110.
4. Keener, E.R.: Flow Separation on Symmetric Forebodies, NASA TM-86016, Jan. 1986.
5. Lamount, P.J.: Pressures Around an Inclined Ogive Cylinder with Laminar, Transitional, or Turbulent Separation, *AIAA Journal*, vol. 20, No. 11, Nov. 1982, pp. 1492-1499.
6. Sorenson, R.L.: A Computer Program to Generate Two-Dimensional Grids About Airfoils and Other Shapes by the Use of Poisson's Equation. NASA TM-81198, May 1980.
7. Kwak, D.; and Chang, J.L.C.: A Three Dimensional Incompressible Flow Solver, Parts 1 and 2., Notes for the Workshop on CFD in Aerospace Design Workshop on CFD in Aerospace Design, U. of Tenn. Space I., Tullahoma, Tenn., 1985.

8. Rogers, S.E.; and Kwak, D.; and Kaul, U.: On the Accuracy of the Pseudo-compressibility Method in Solving the Incompressible Navier-Stokes Equations, AIAA paper 85-1689, July 1985.
9. Peake, D.J.; and Tobak, M.: Three-Dimensional Interactions and Vortical Flows With Emphasis on High Speeds, AGARDograph No. AG-252, July 1980.

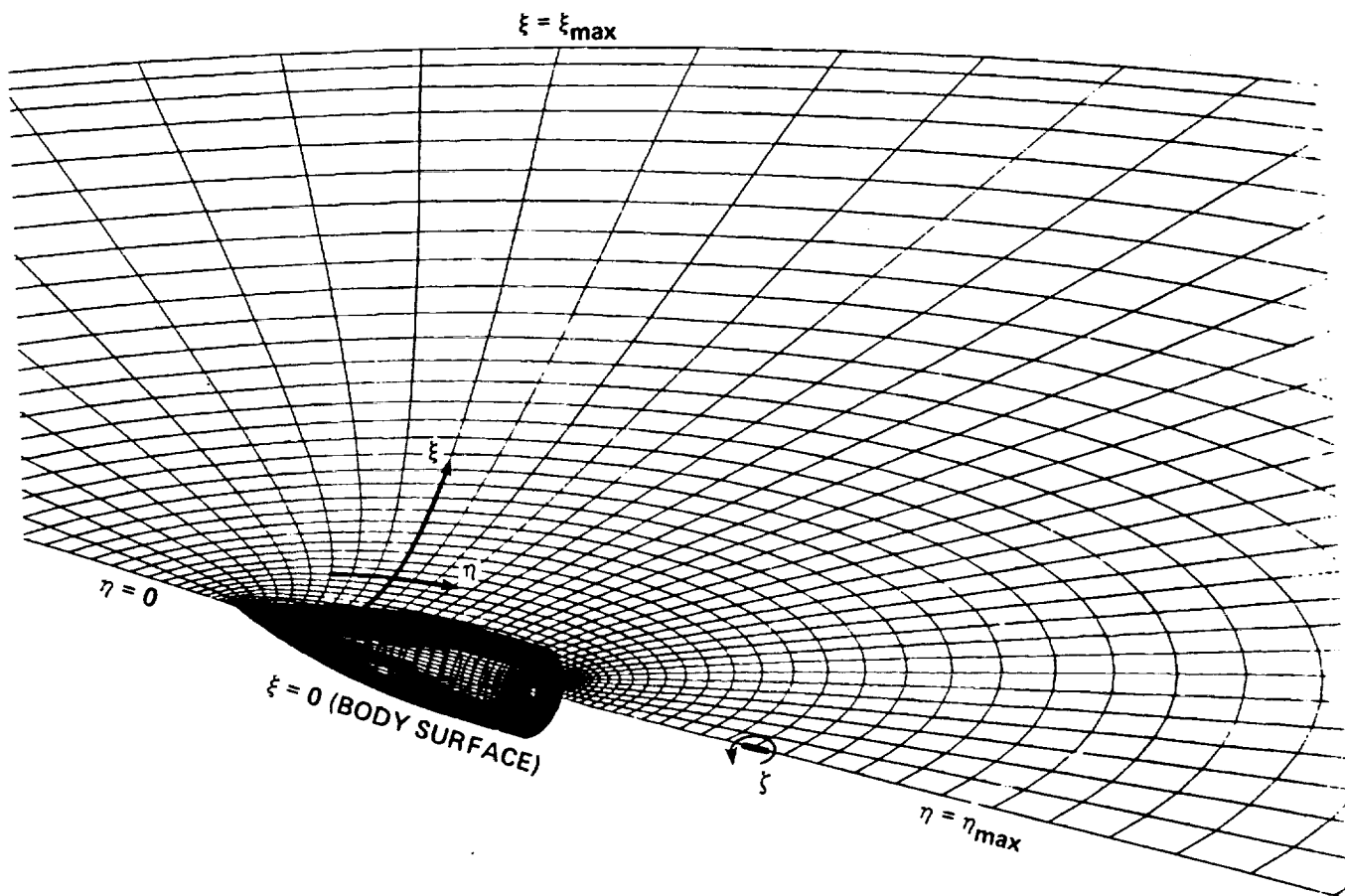


Figure 1.- Perspective view of the wrapped computational mesh.

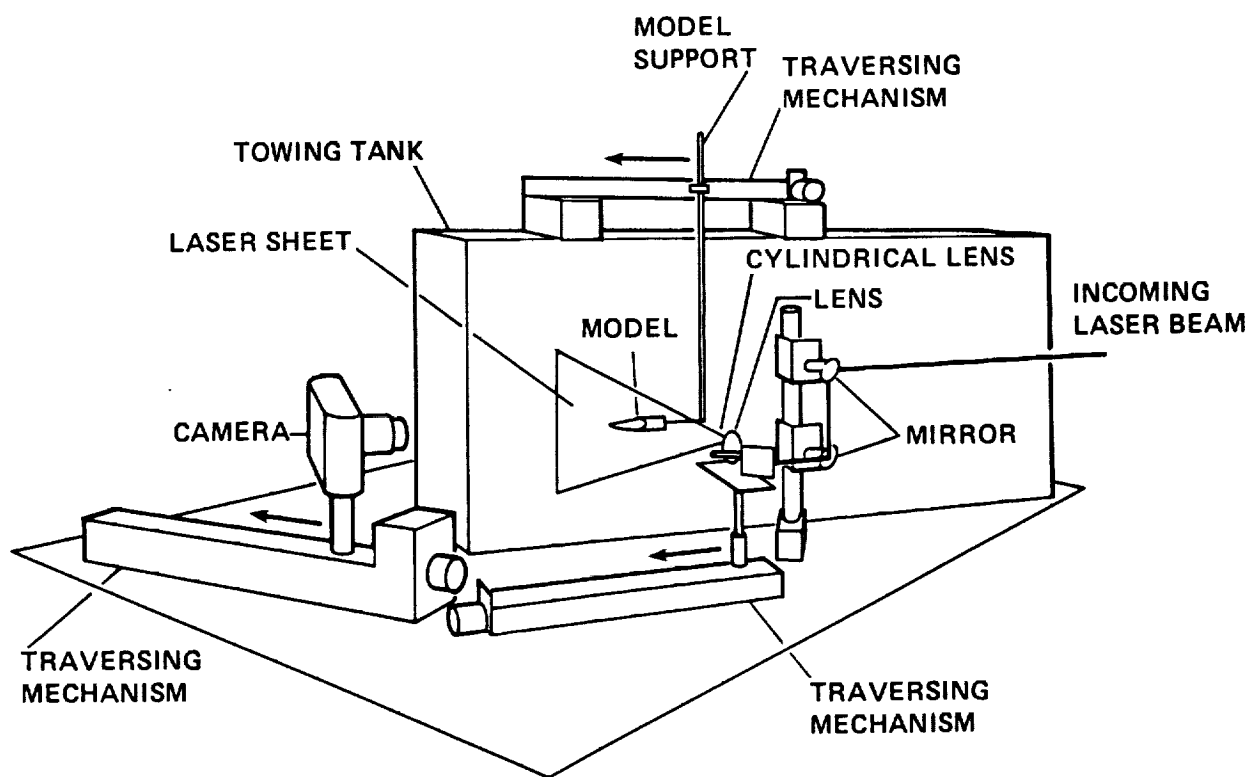


Figure 2.- Perspective view of the towing tank with model.

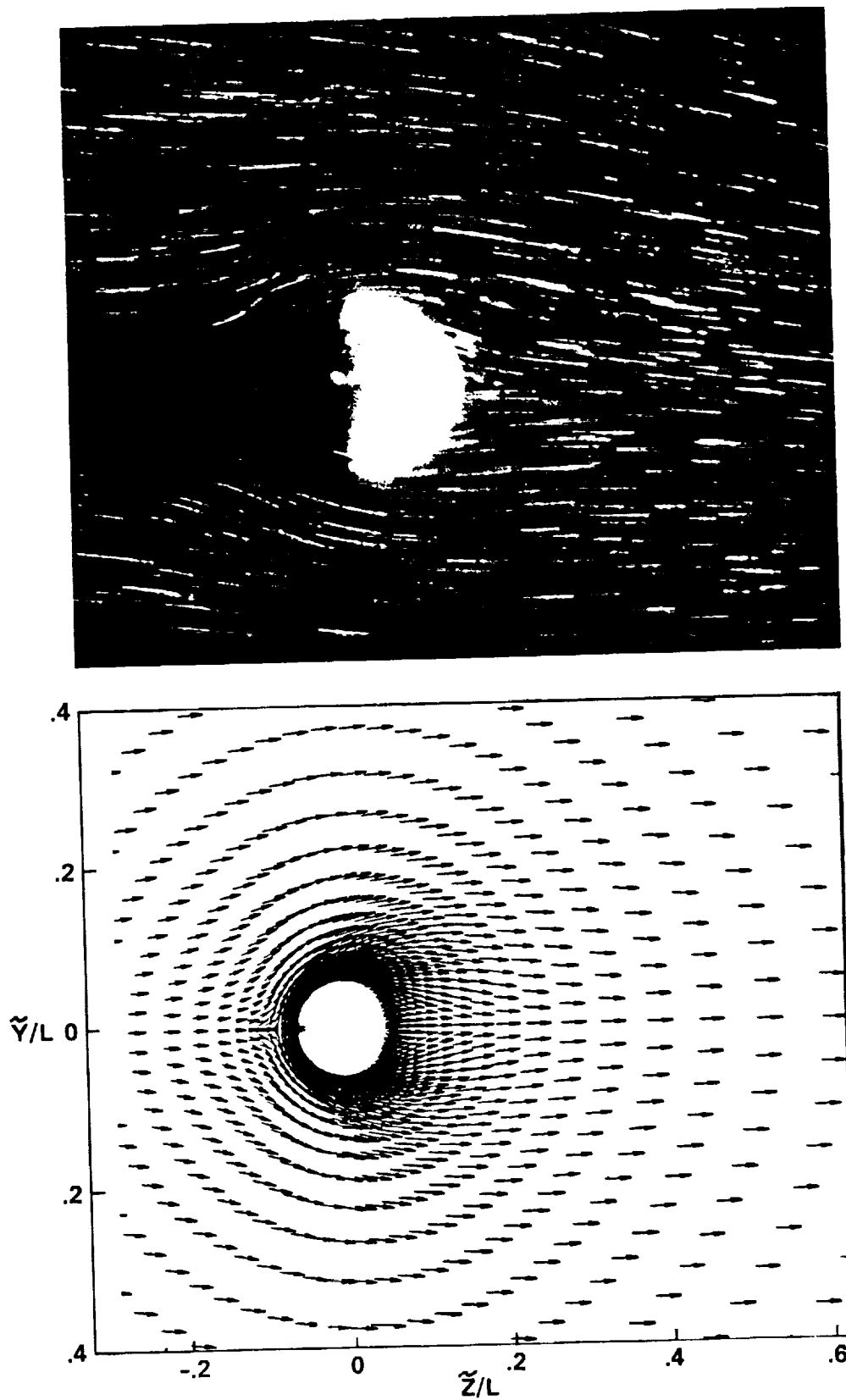


Figure 3a.- Comparison of computed and visualized crossflow velocity vectors
at $X/L = 0.2$. $\alpha = 30^\circ$.

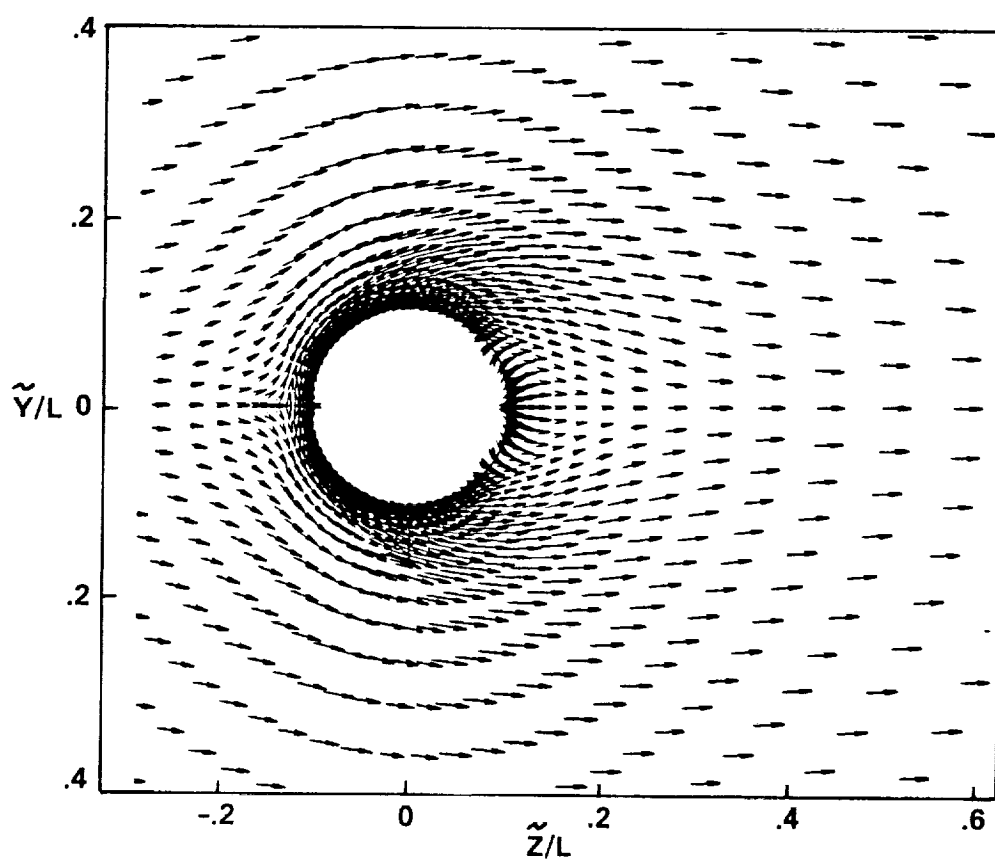
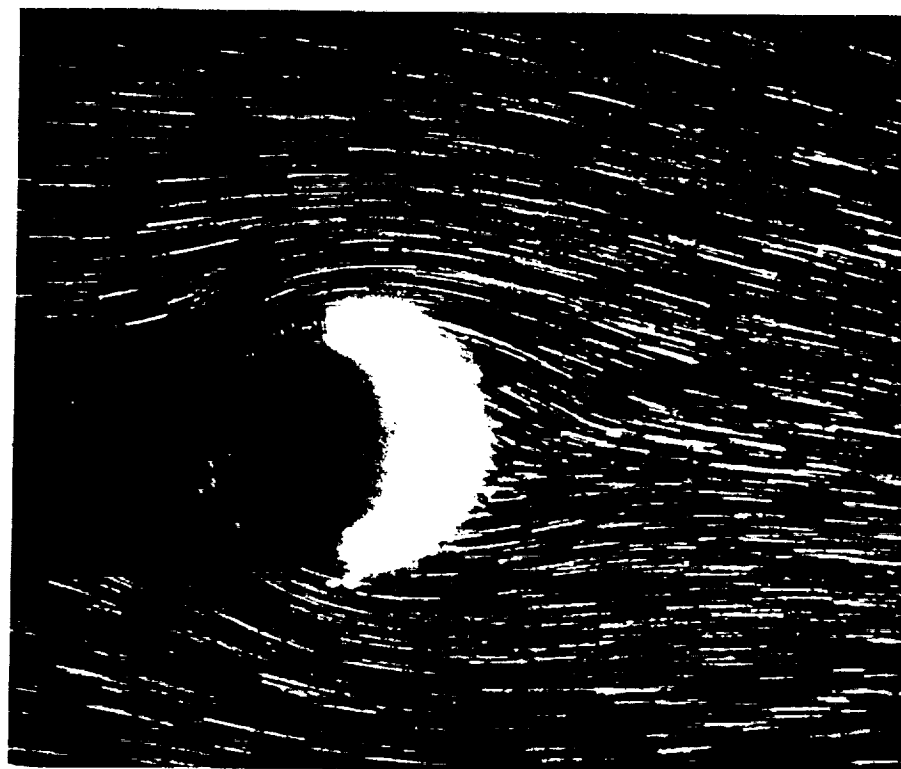


Figure 3b.- Comparison of computed and visualized crossflow velocity vectors
at $X/L = 0.4$, $\alpha = 30^\circ$.

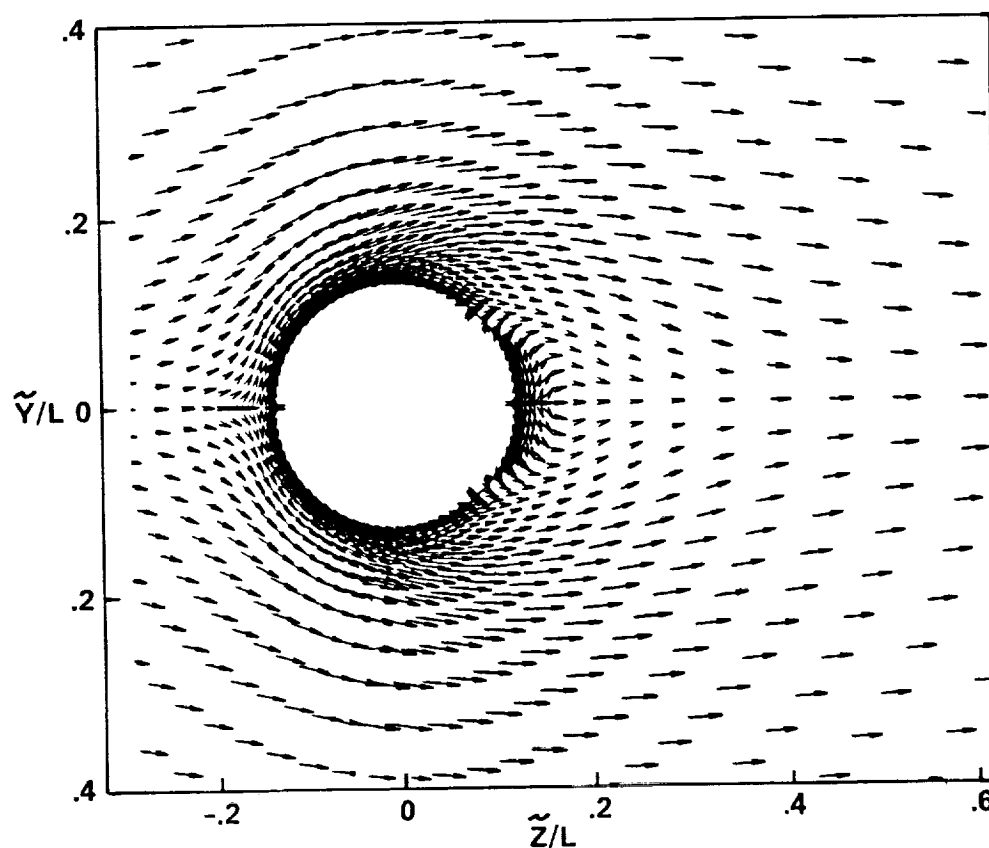
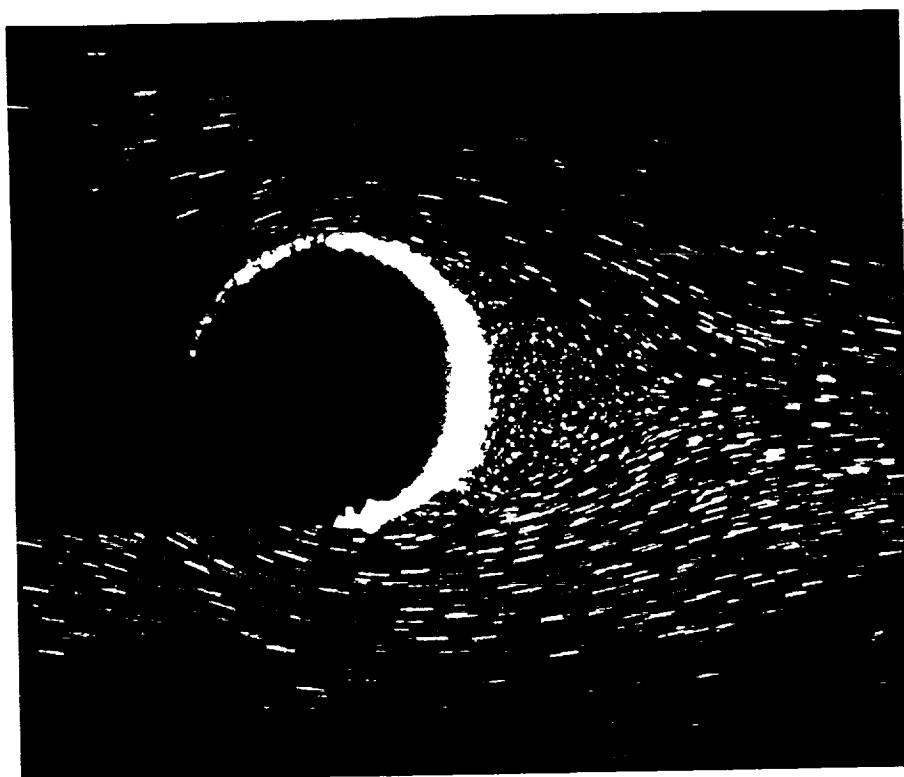


Figure 3c.- Comparison of computed and visualized crossflow velocity vectors
at $X/L = 0.6$, $\alpha = 30^\circ$.

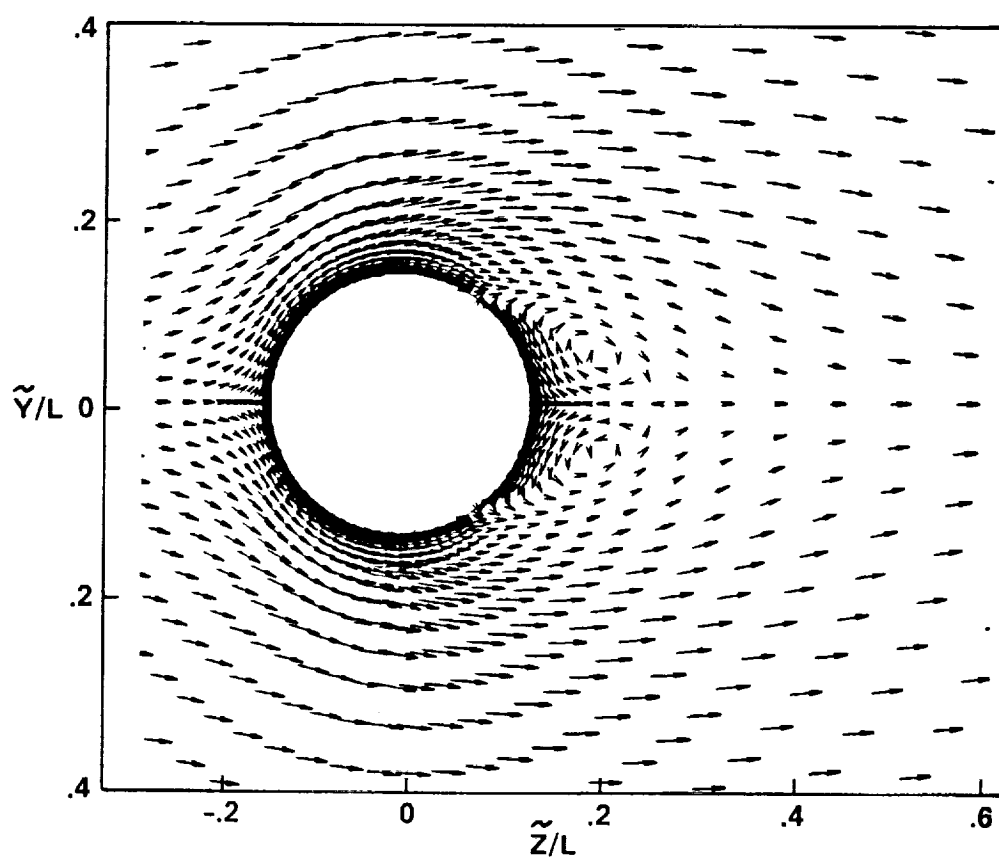
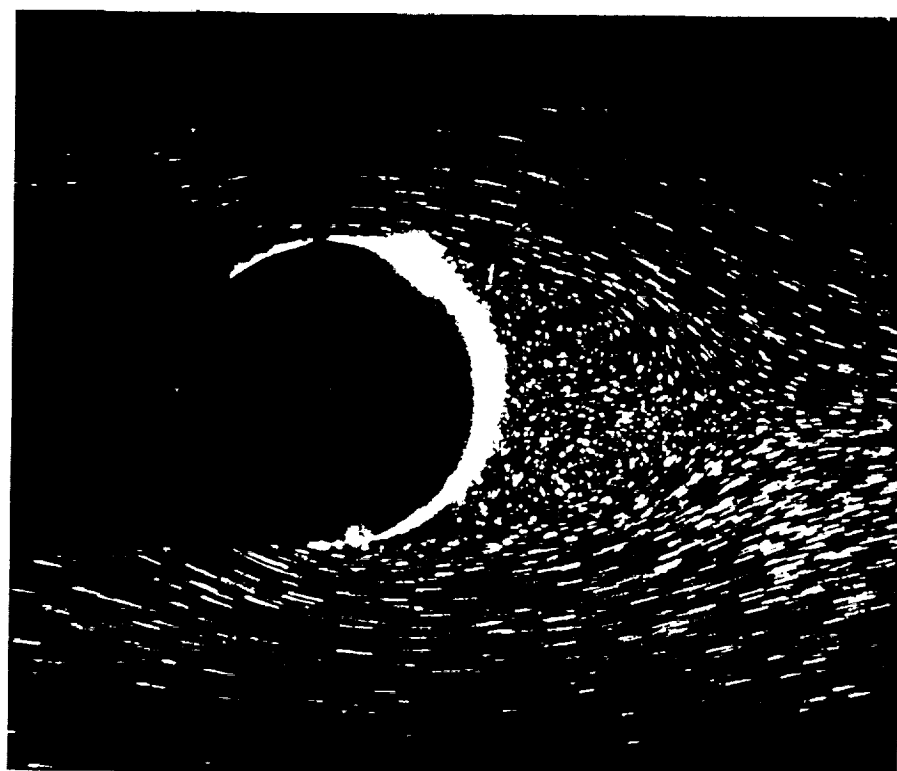


Figure 3d.- Comparison of computed and visualized crossflow velocity vectors
at $X/L = 0.8$, $\alpha = 30^\circ$.

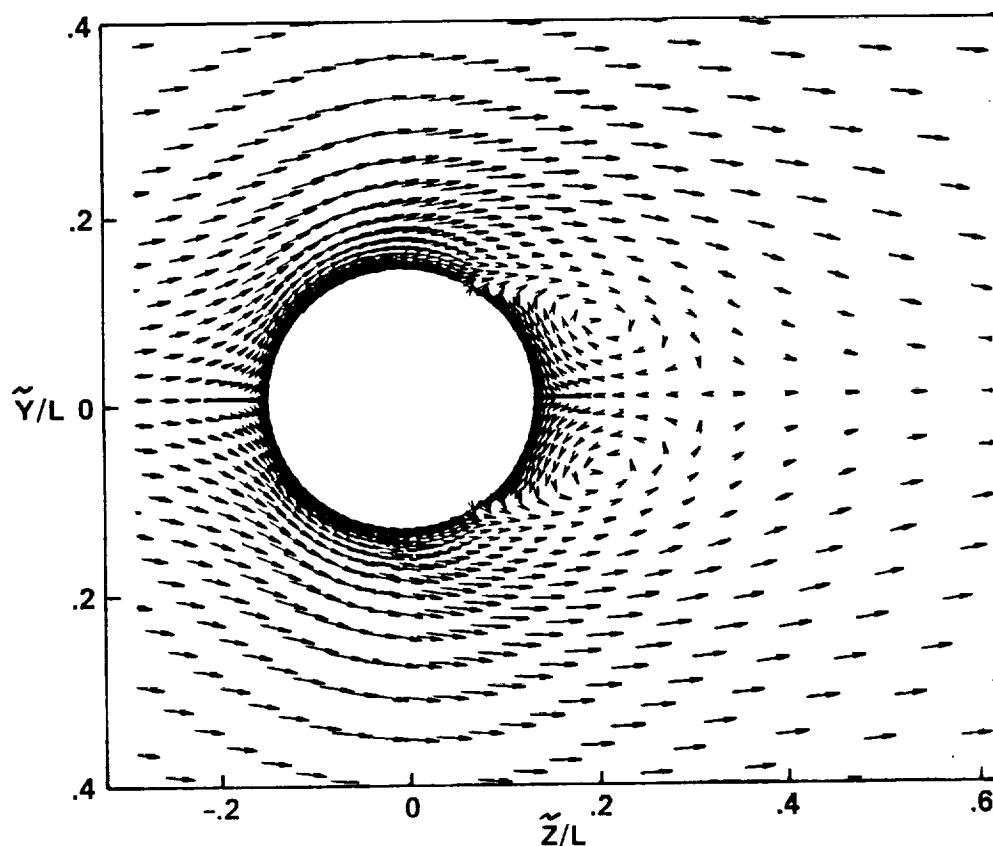
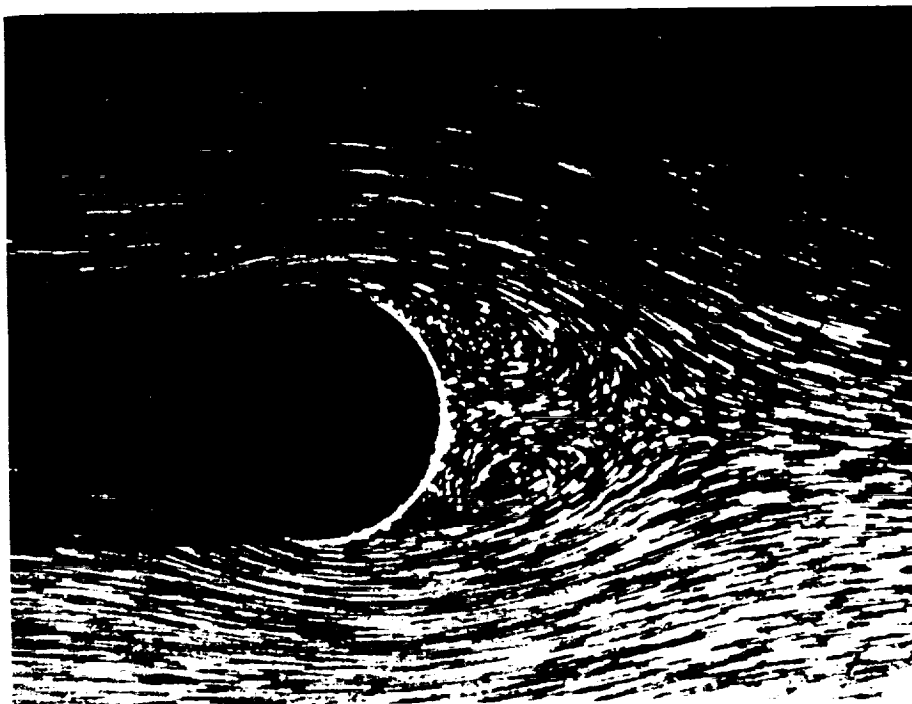


Figure 3e.- Comparison of computed and visualized crossflow velocity vectors
at $X/L = 0.95$, $\alpha = 30^\circ$.

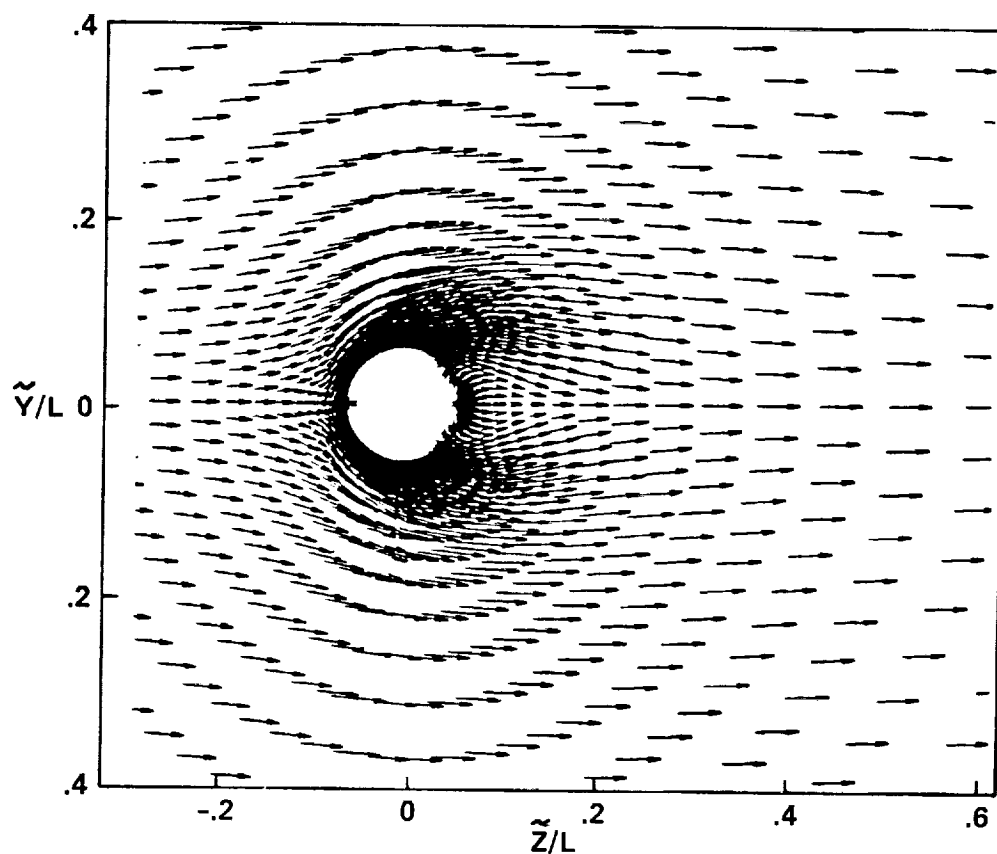
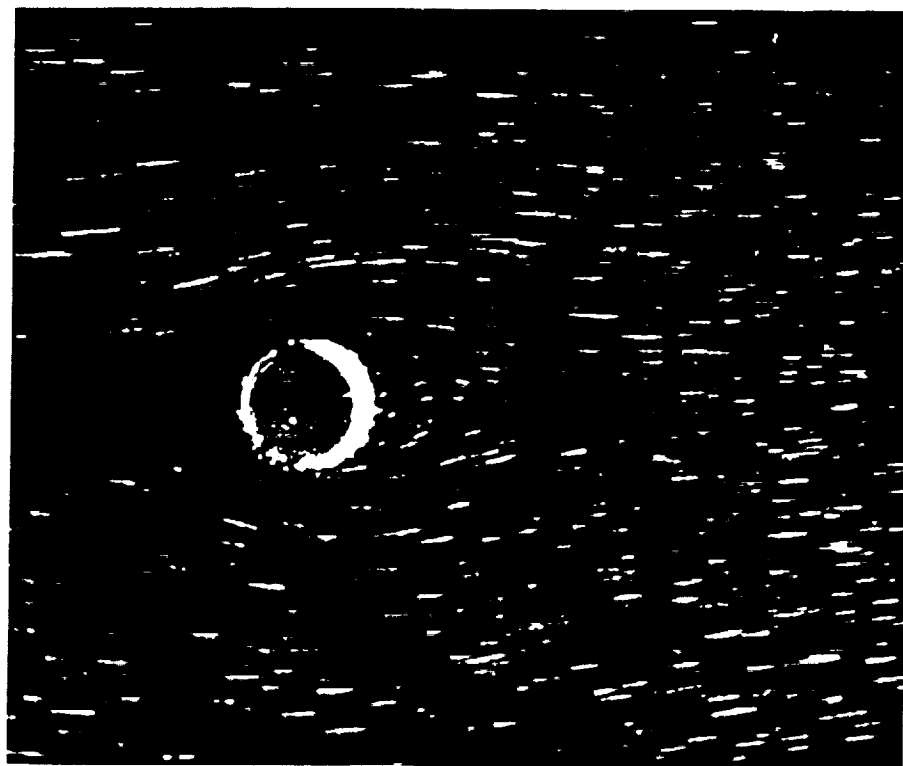


Figure 4a.- Comparison of computed and visualized crossflow velocity vectors
at $X/L = 0.2$, $\alpha = 45^\circ$.

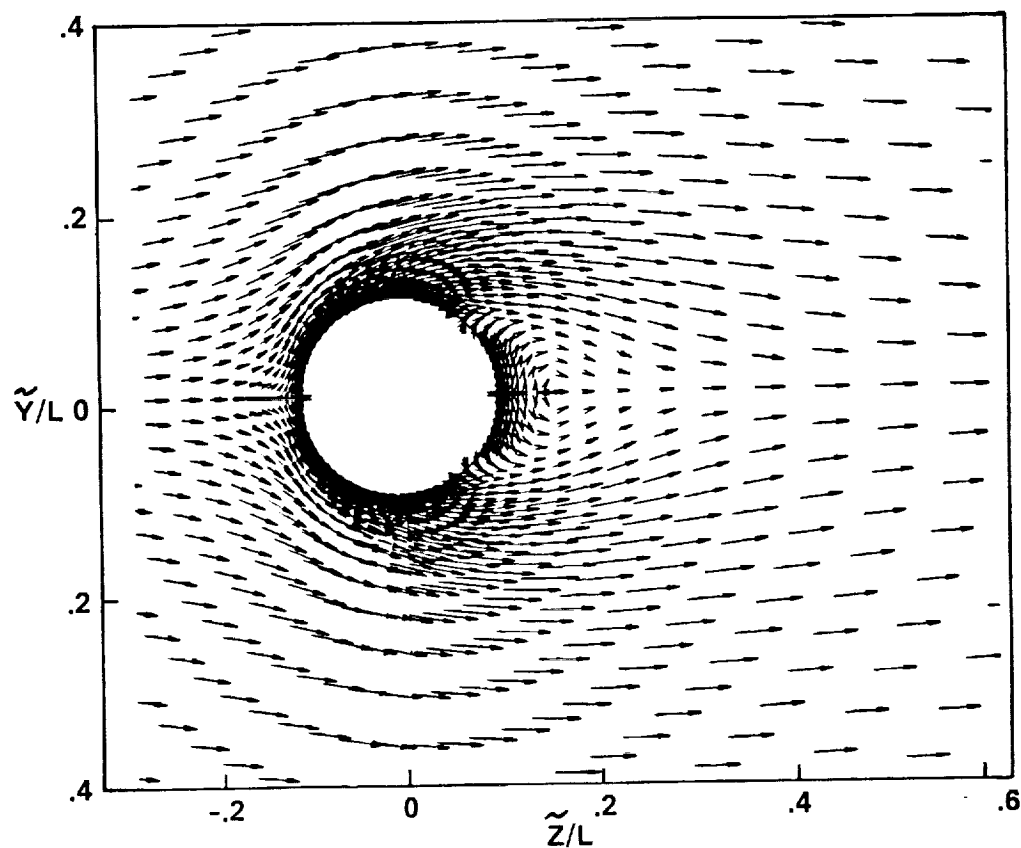
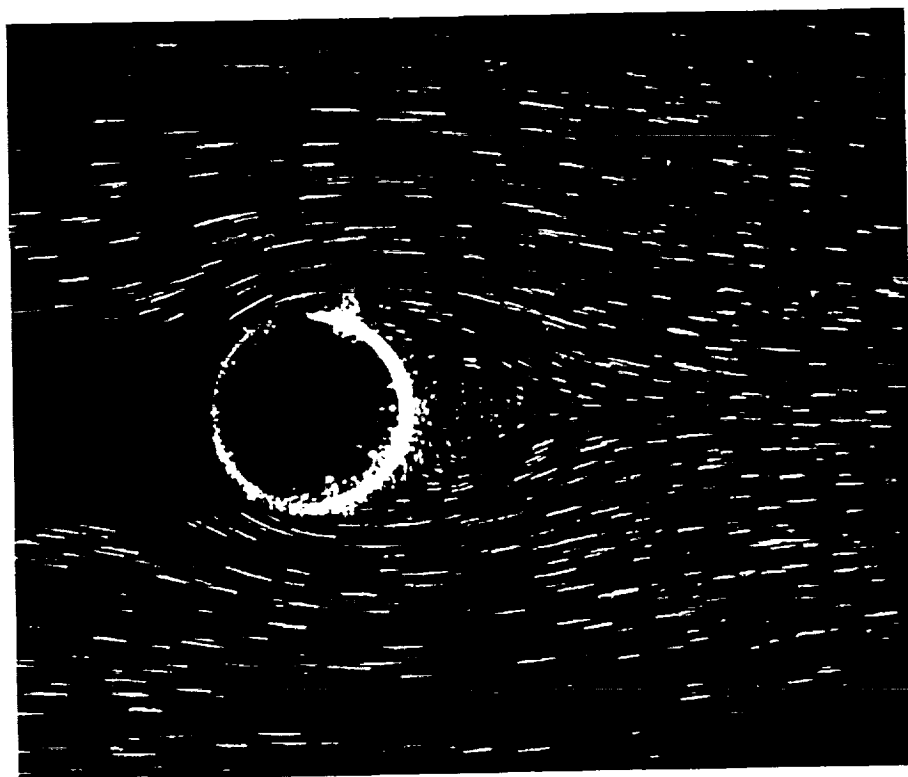


Figure 4b.- Comparison of computed and visualized crossflow velocity vectors
at $X/L = 0.4$, $\alpha = 45^\circ$.

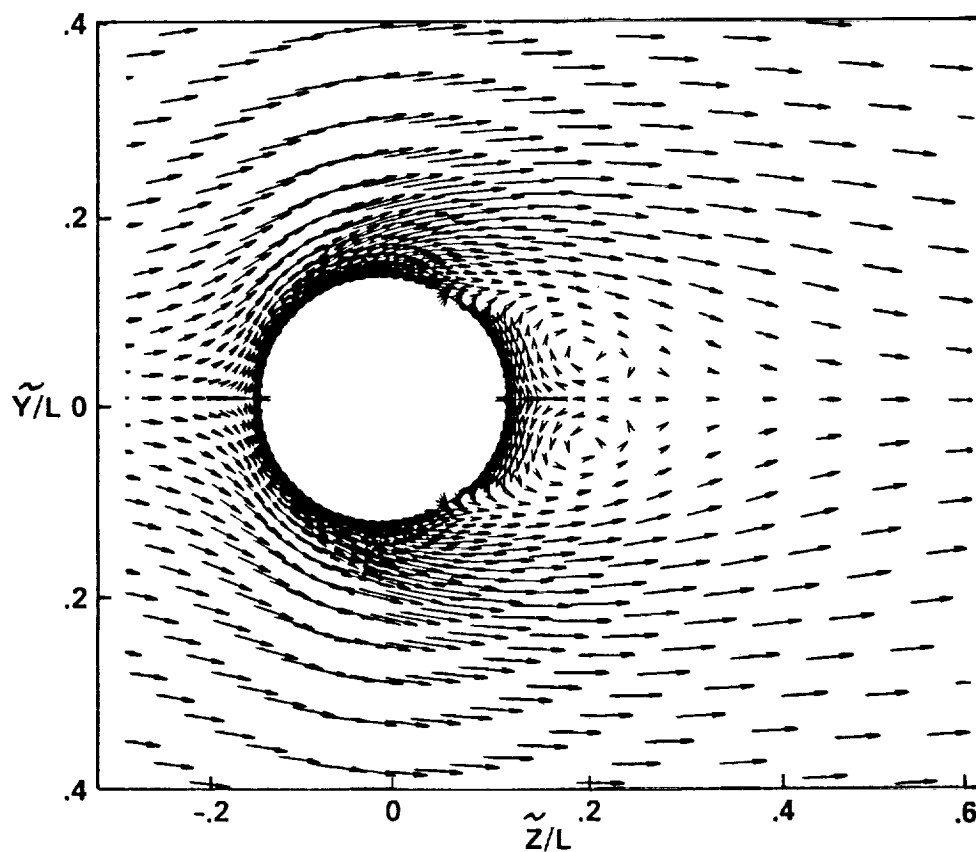


Figure 4c.- Comparison of computed and visualized crossflow velocity vectors
at $X/L = 0.6$, $\alpha = 45^\circ$.

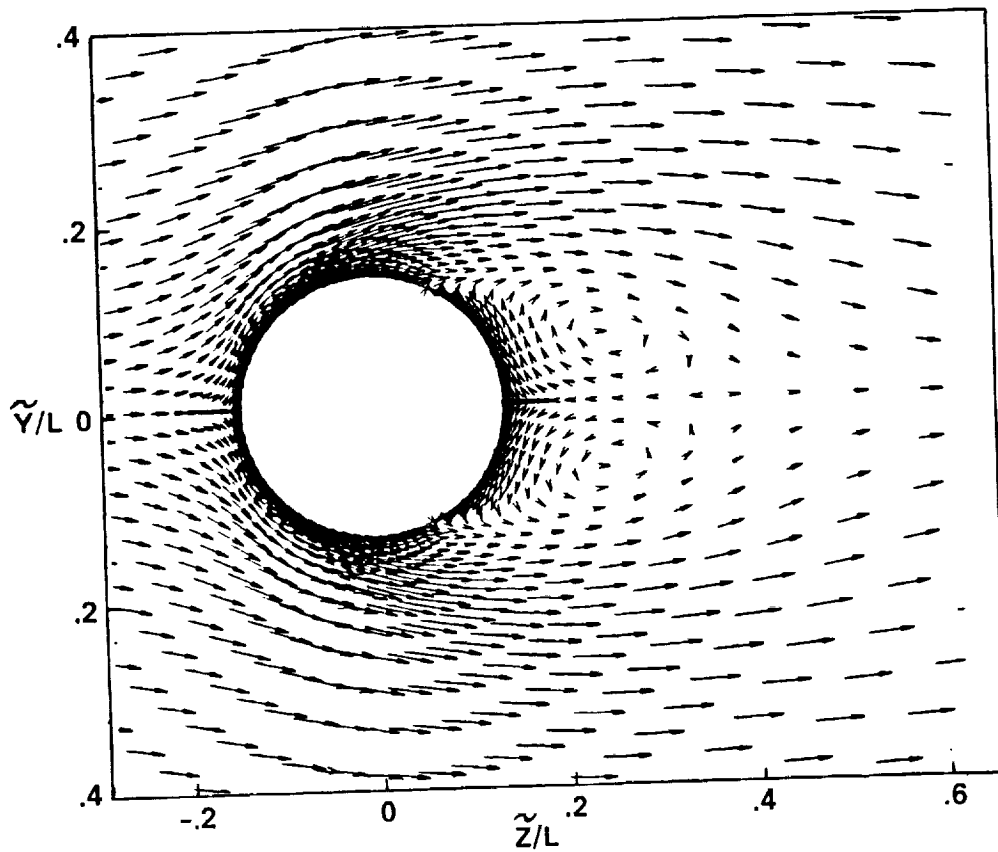
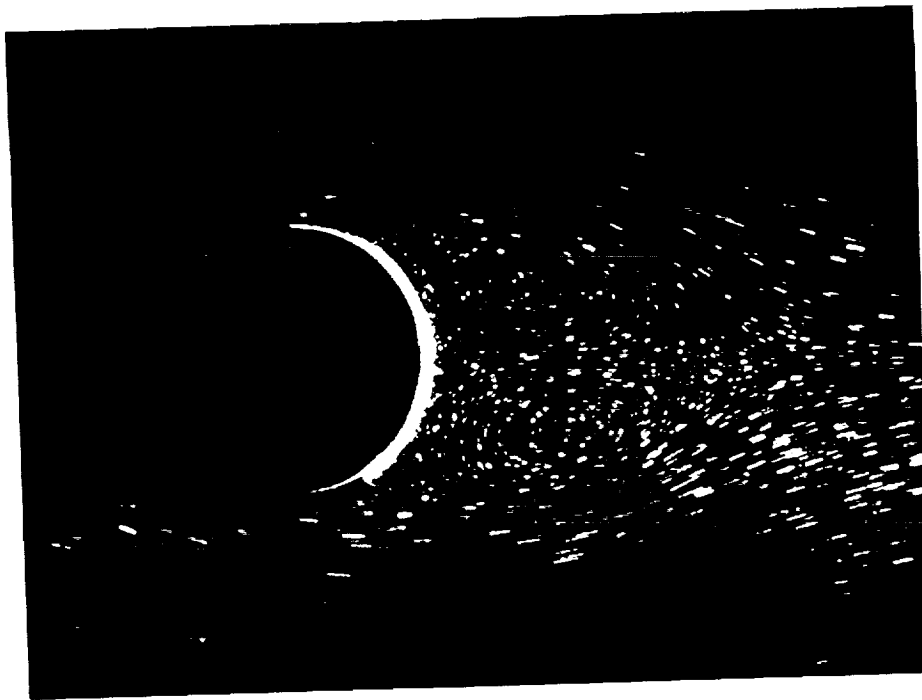


Figure 4d.- Comparison of computed and visualized crossflow velocity vectors
at $X/L = 0.8$, $\alpha = 45^\circ$.

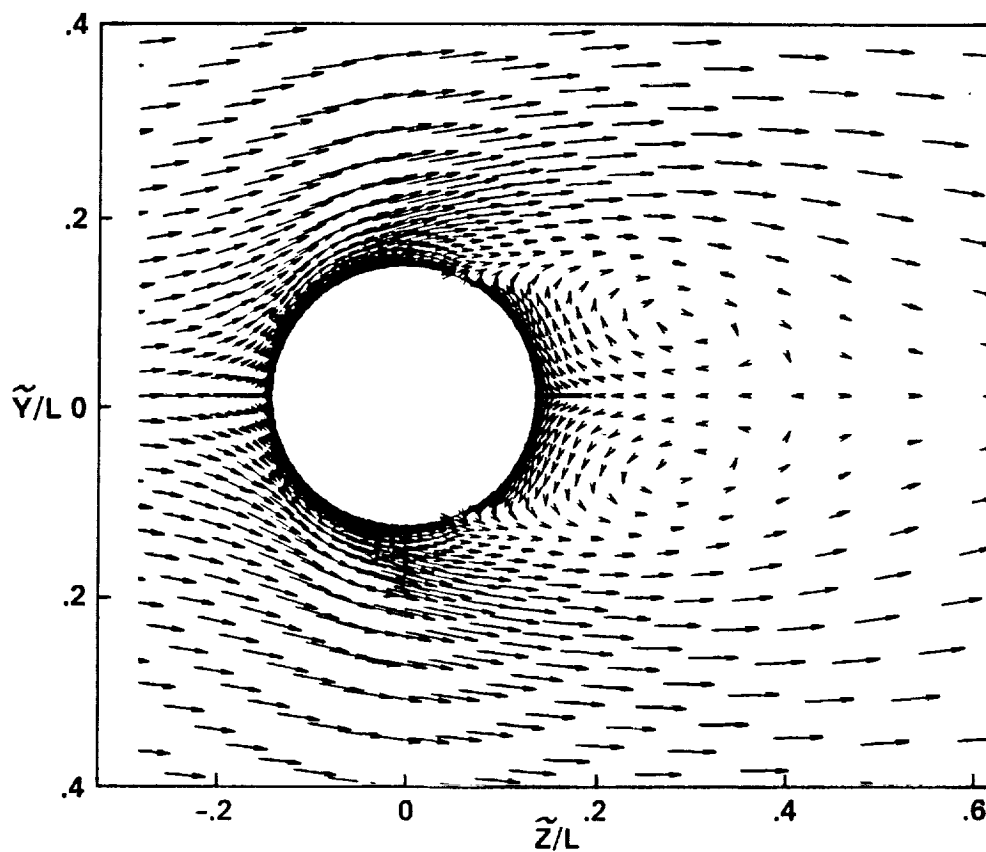
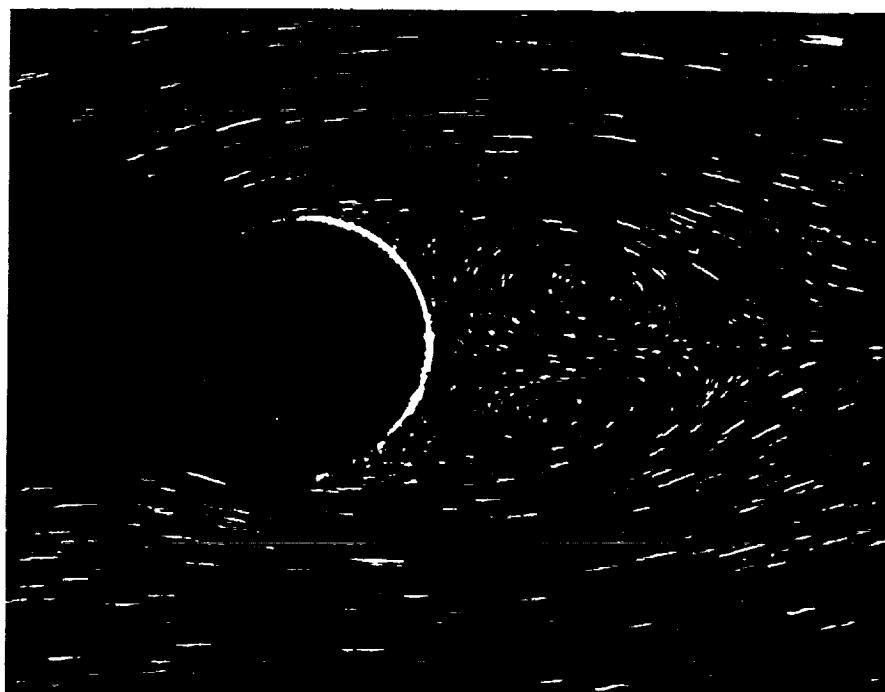


Figure 4e.- Comparison of computed and visualized crossflow velocity vectors
at $X/L = 0.95$, $\alpha = 45^\circ$.

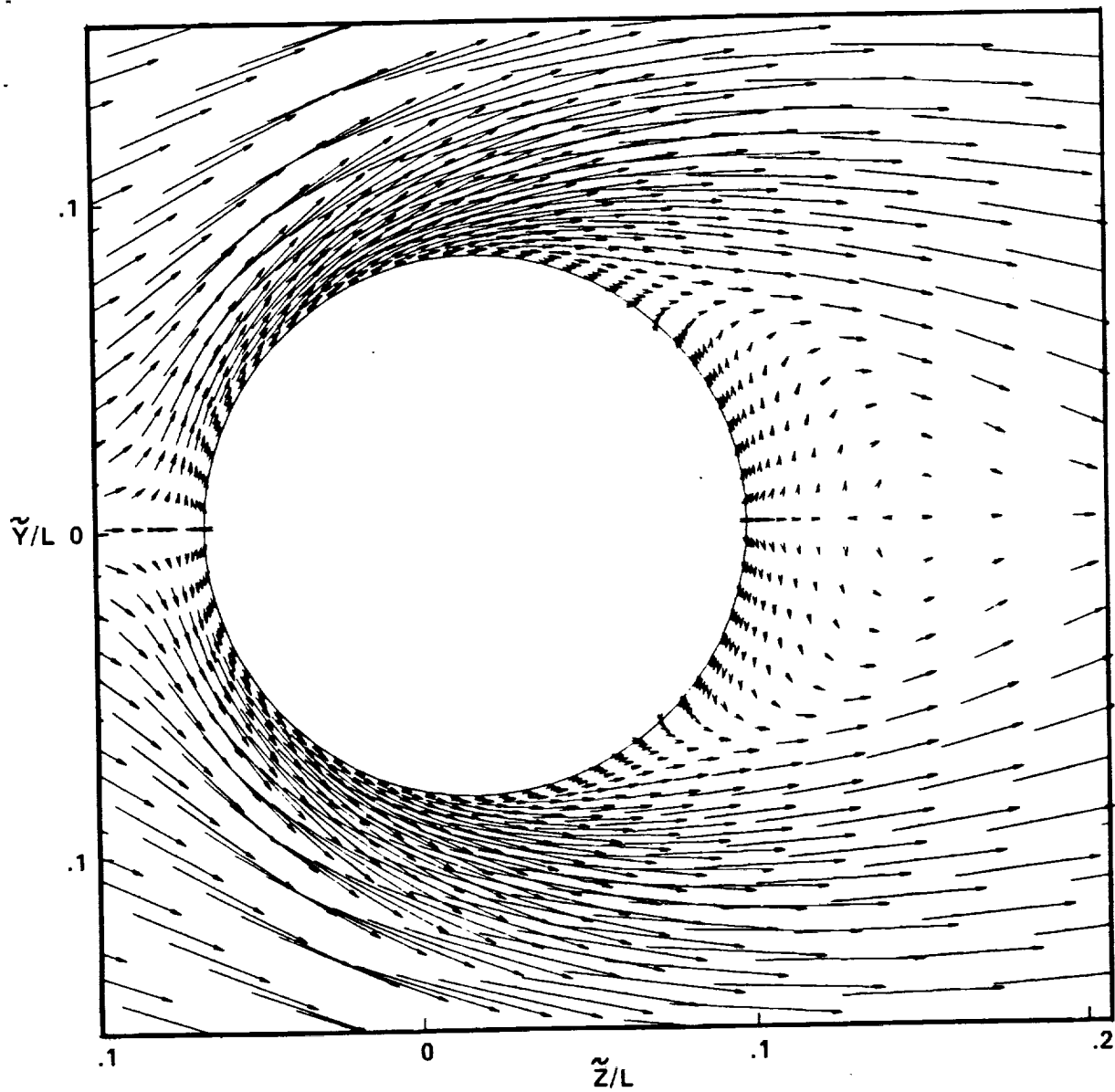


Figure 5.- Closeup of the velocity field near the surface in the crossflow plane at $X/L = 0.4$, $\alpha = 45^\circ$.

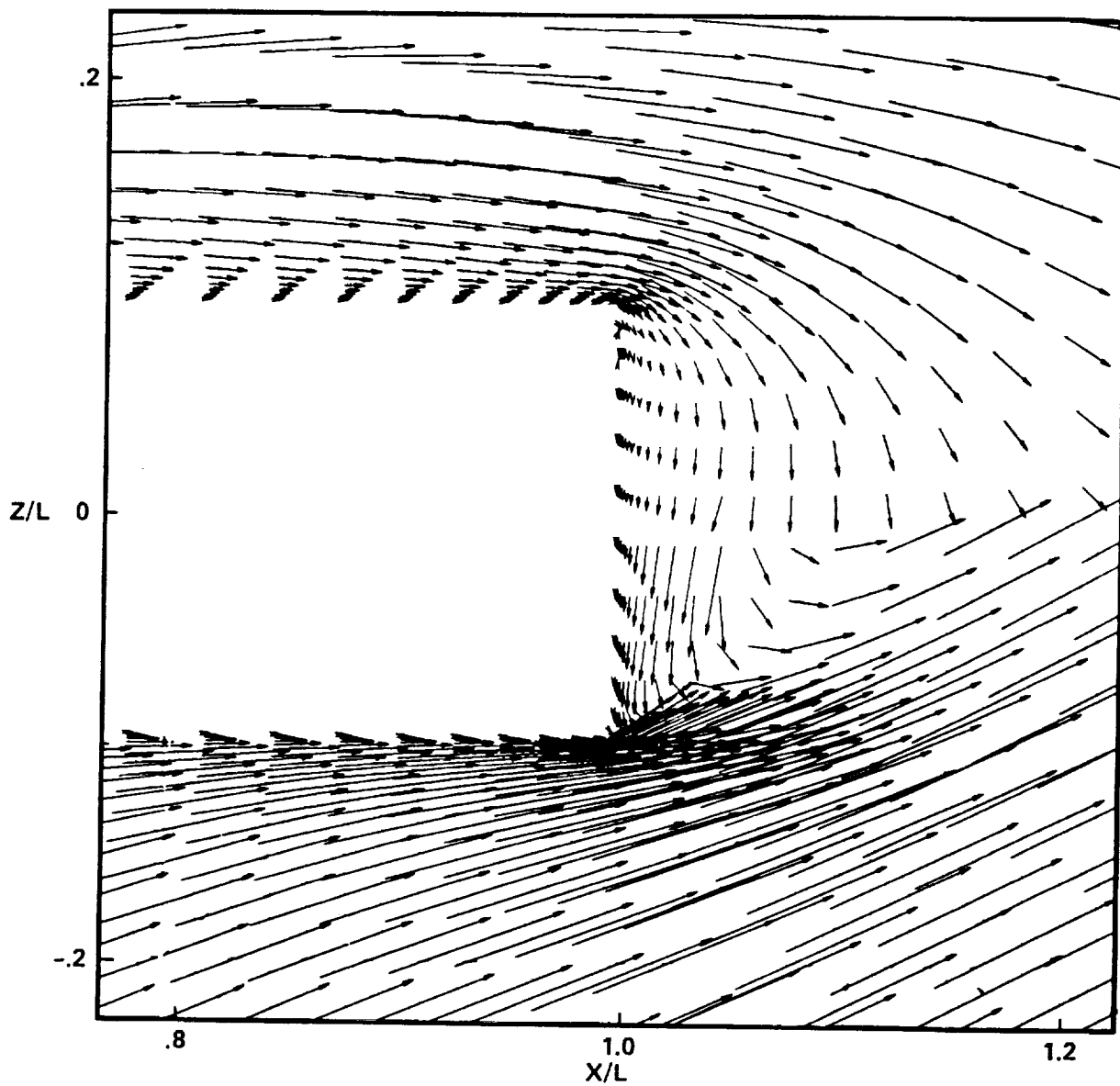


Figure 6.- Aft symmetry plane flow at $\alpha = 30^\circ$.

ORIGINAL PAGE IS
OF POOR QUALITY

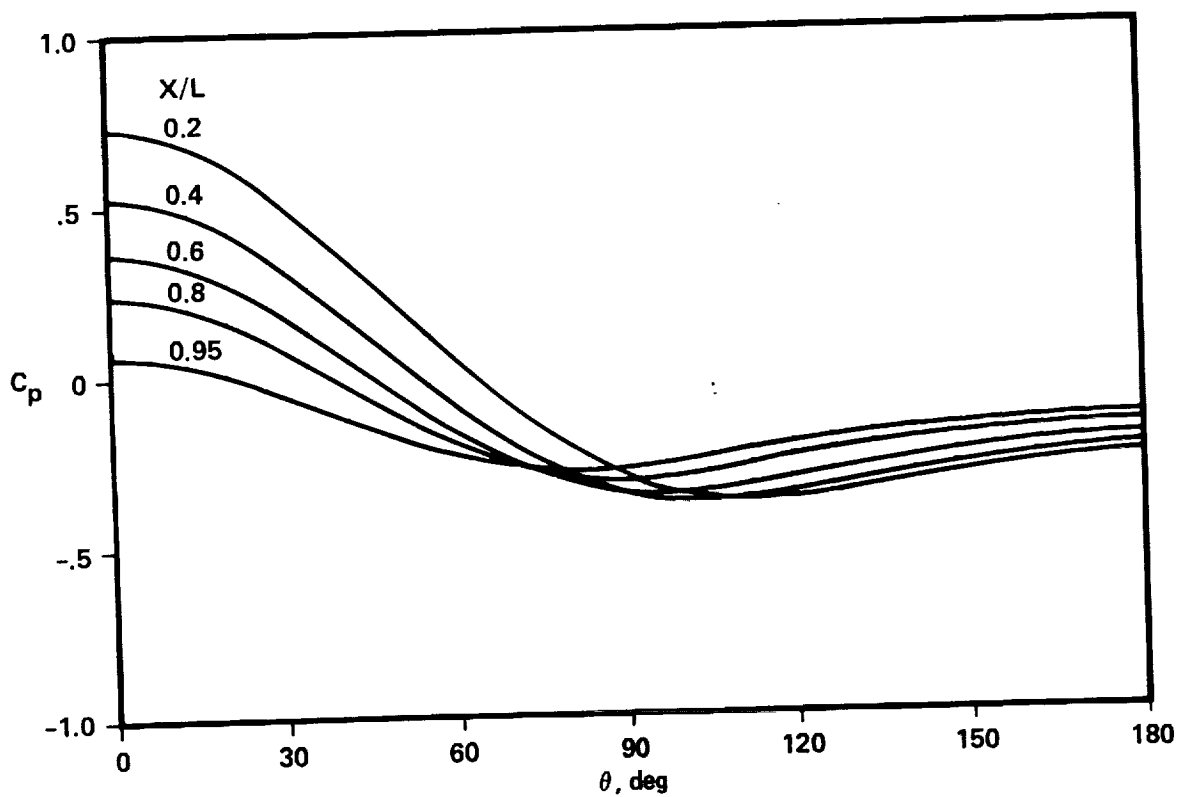


Figure 7.- Circumferential surface pressure in the crossflow plane at various stations along the body at $\alpha = 30^\circ$.

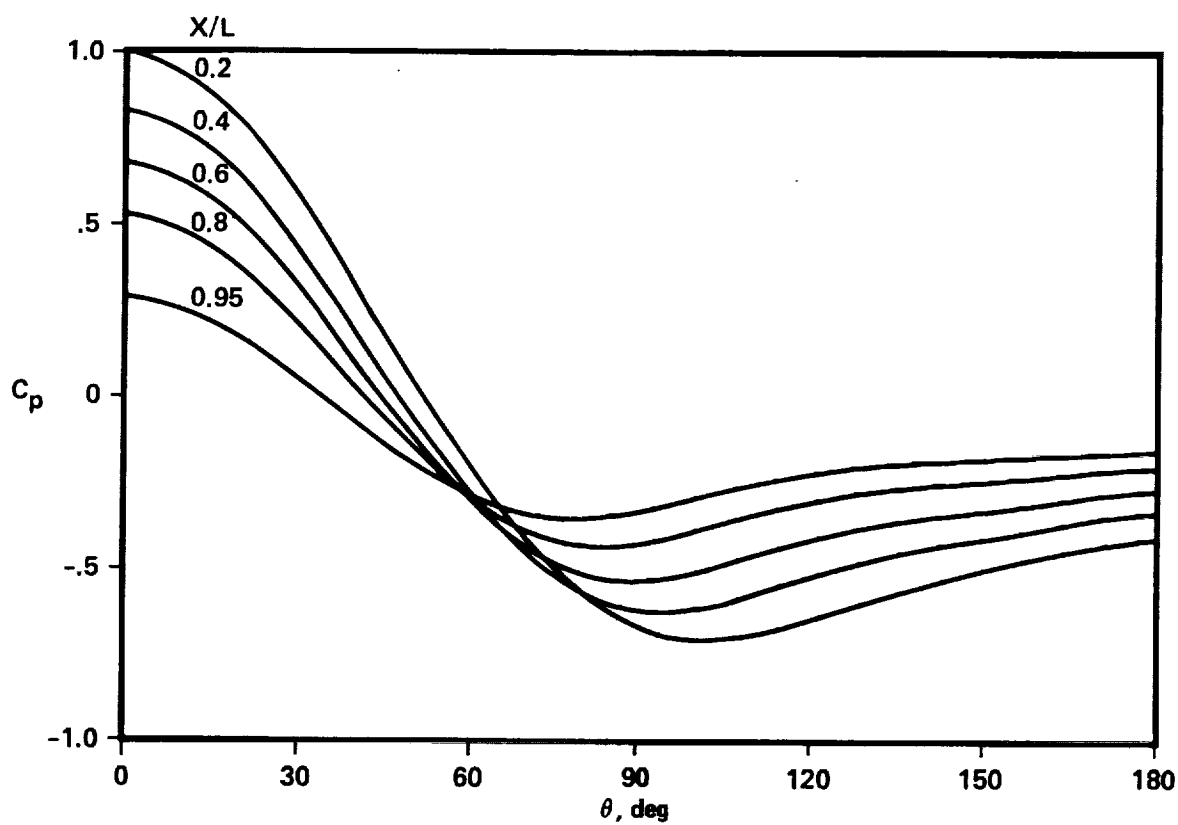


Figure 8.- Circumferential surface pressure in the crossflow plane at various stations along the body at $\alpha = 45^\circ$.

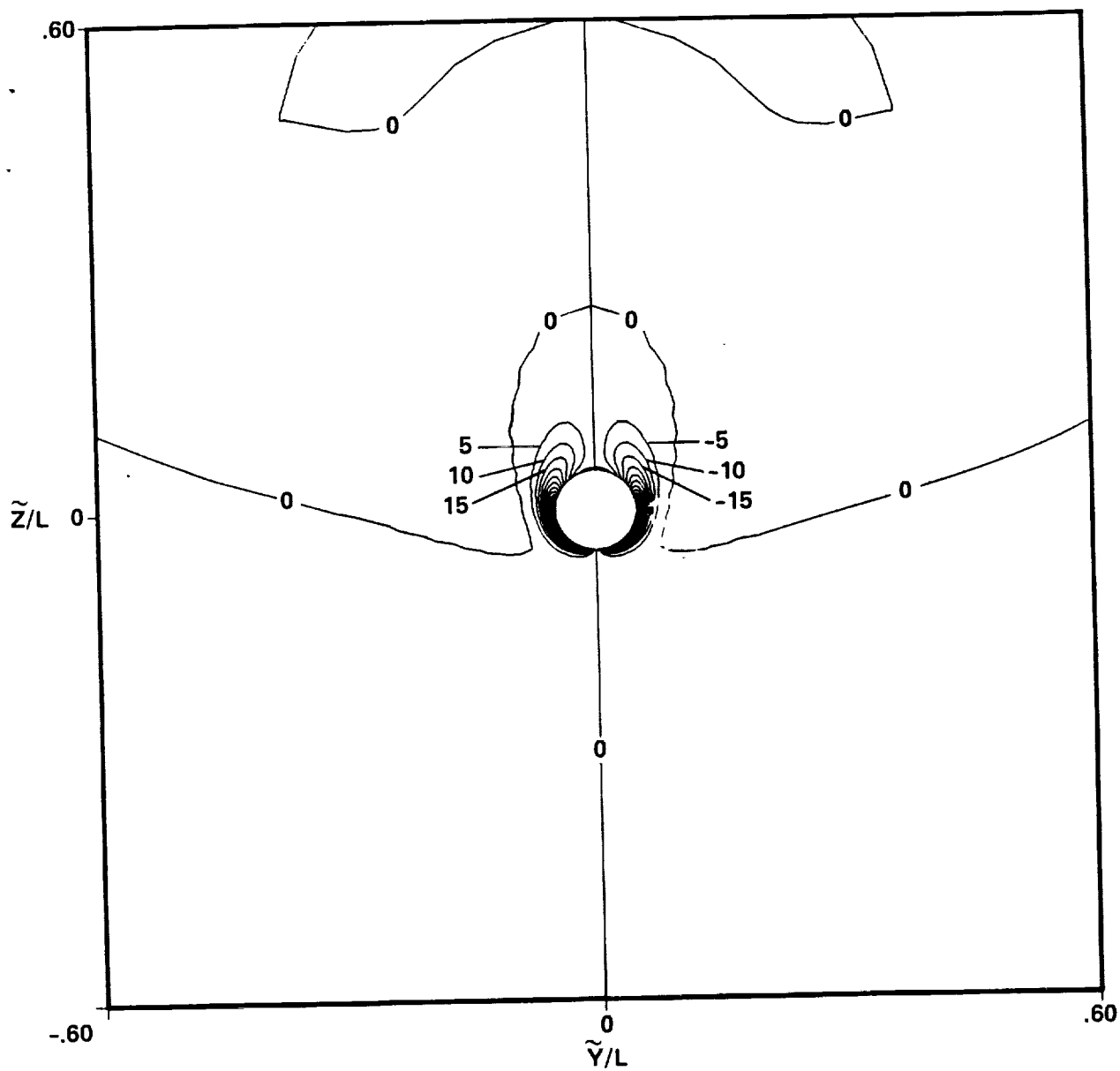


Figure 9a.- Axial vorticity contours in the crossflow plane
at $X/L = 0.2$, $\alpha = 30^\circ$.

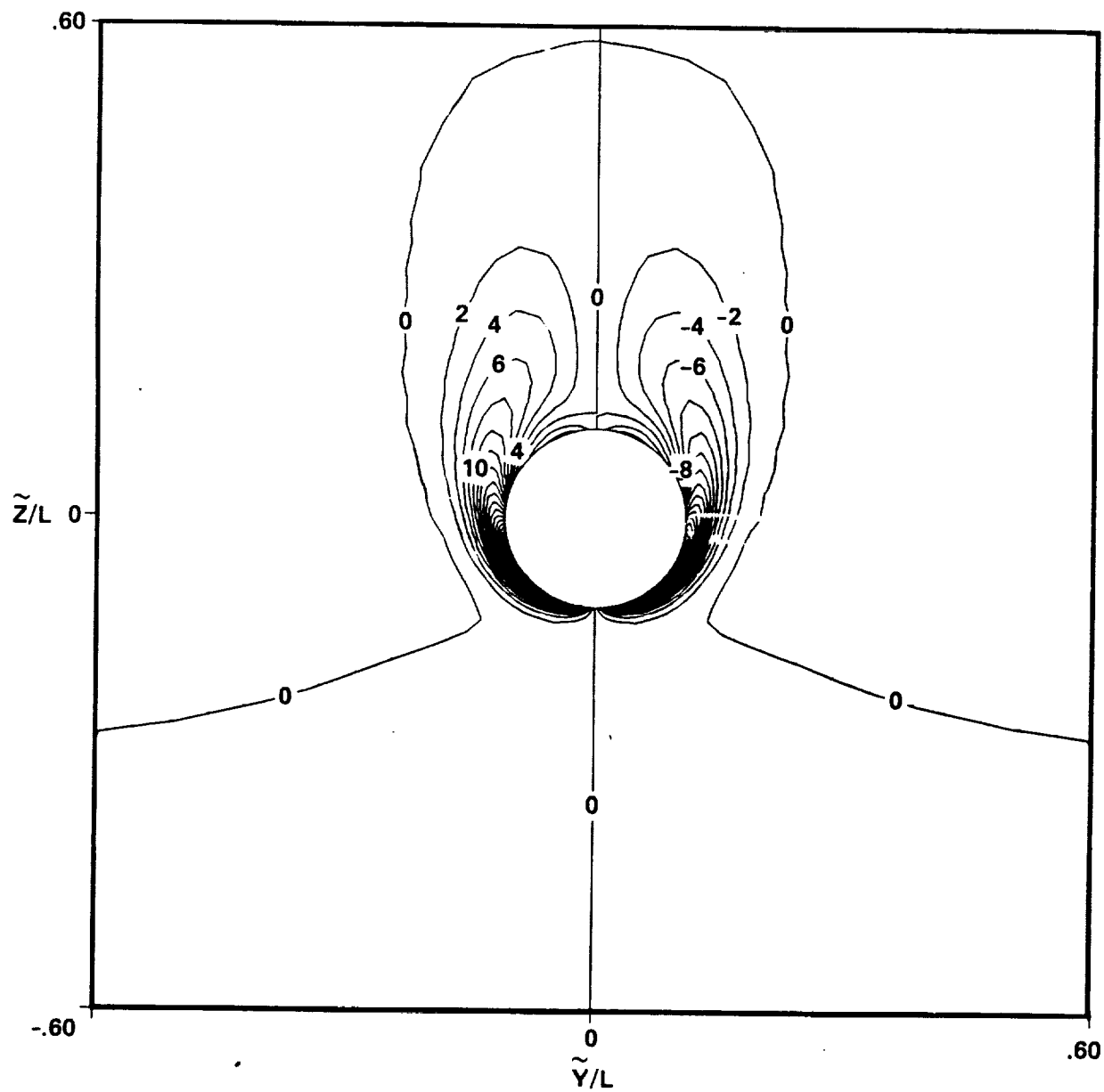


Figure 9b.- Axial vorticity contours in the crossflow plane
at $X/L = 0.95$, $\alpha = 30^\circ$.

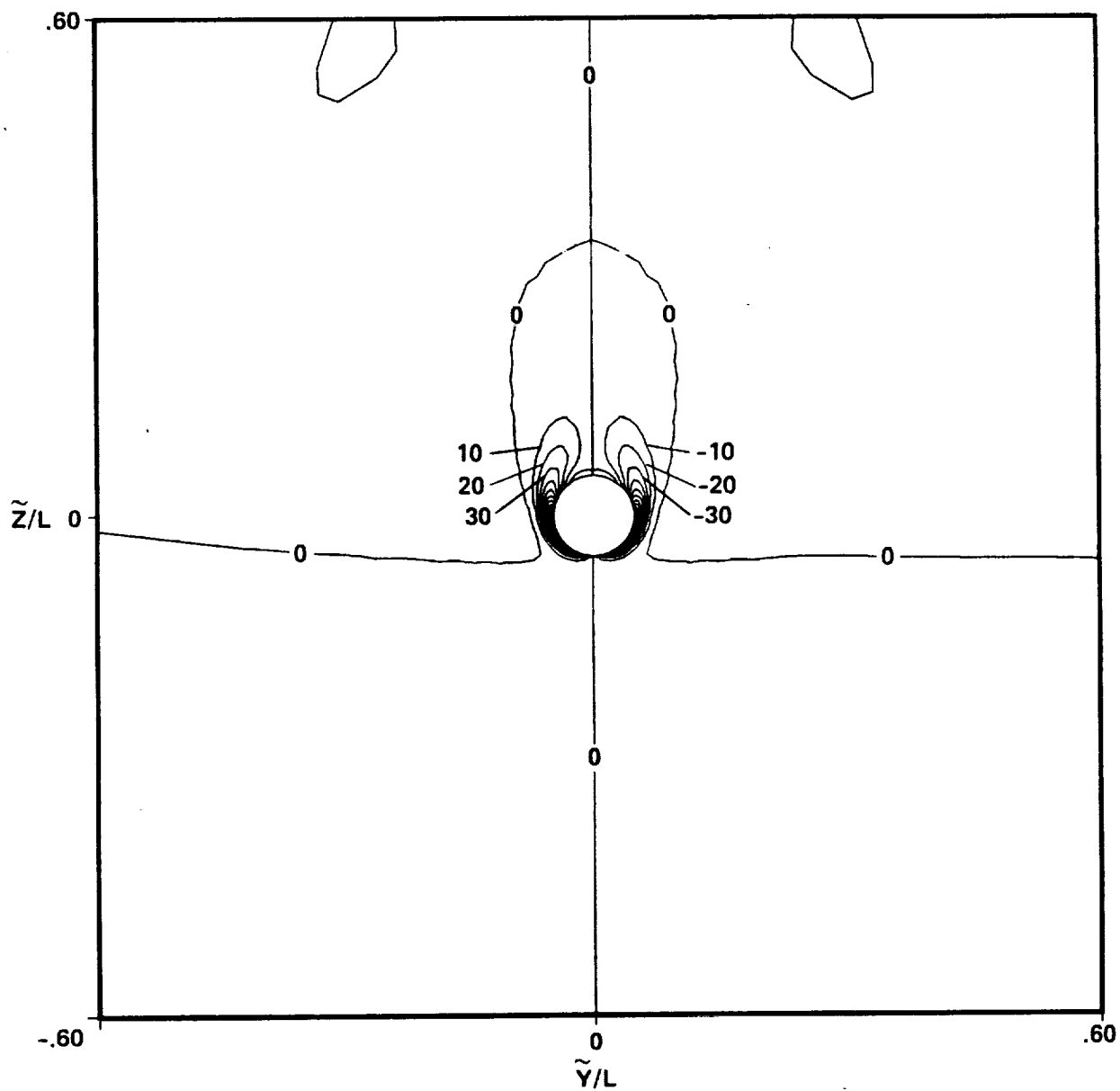


Figure 10a.- Axial vorticity contours in the crossflow plane
at $X/L = 0.2$, $\alpha = 45^\circ$.

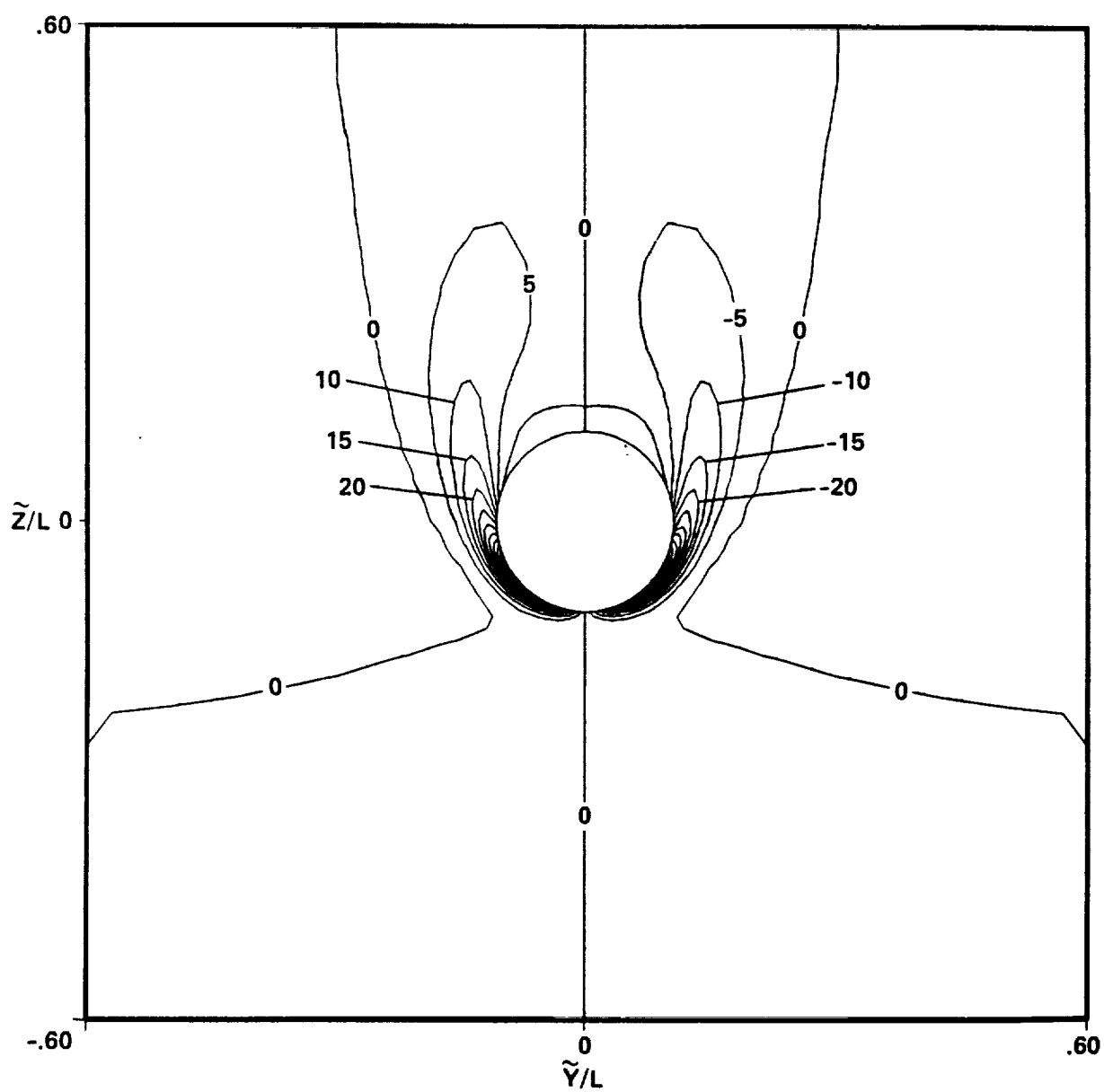


Figure 10b.- Axial vorticity contours in the crossflow plane
at $X/L = 0.95$, $\alpha = 45^\circ$.

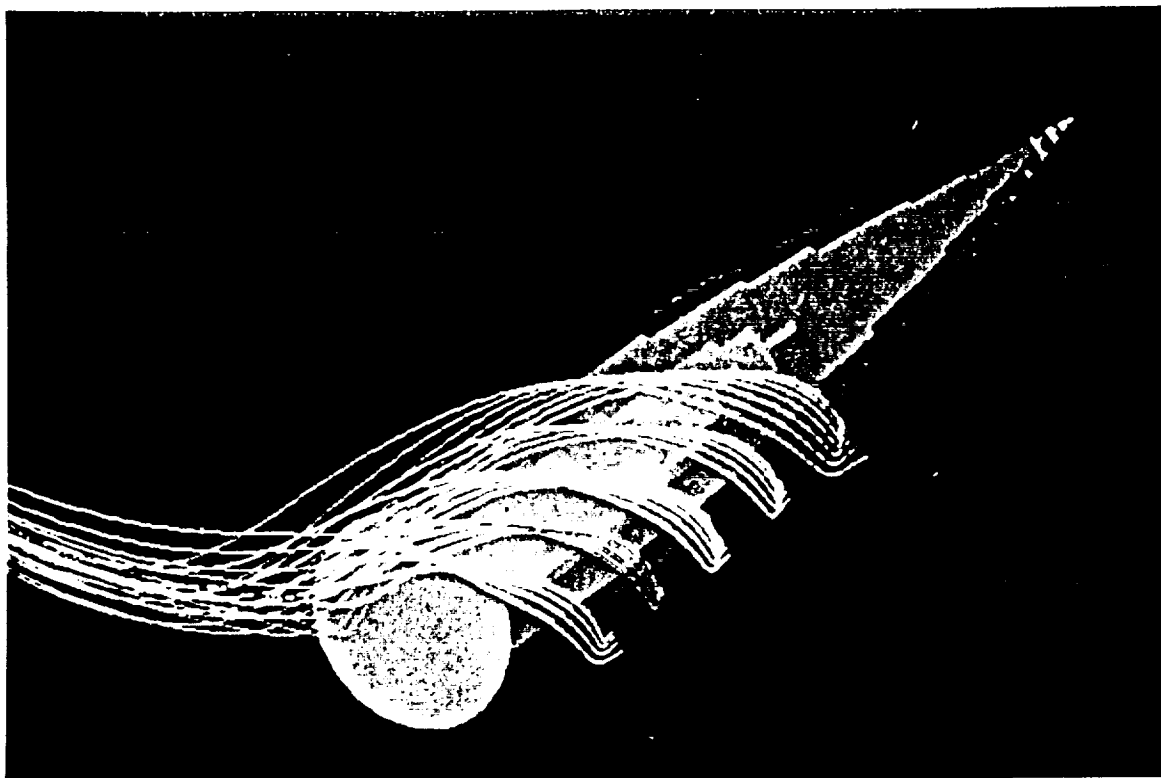


Figure 11.- Computed particle path lines for $\alpha = 30^\circ$.

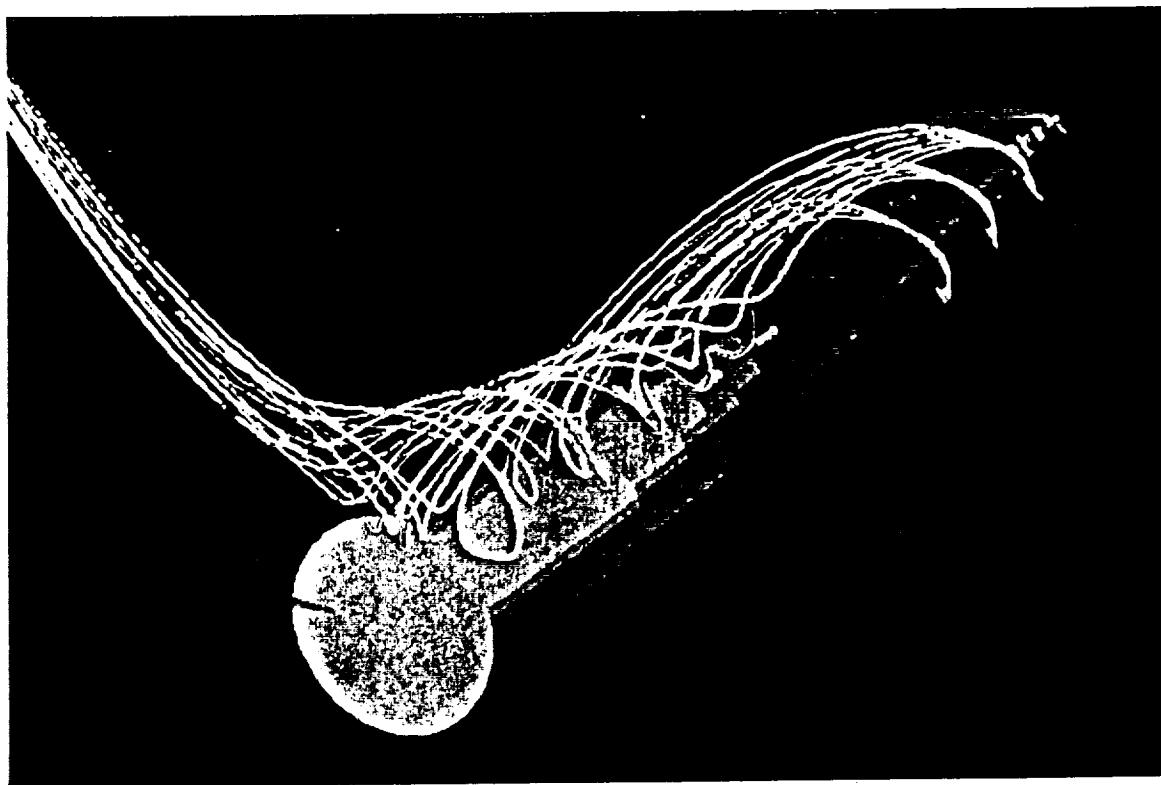


Figure 12.- Computed particle path lines for $\alpha = 45^\circ$.

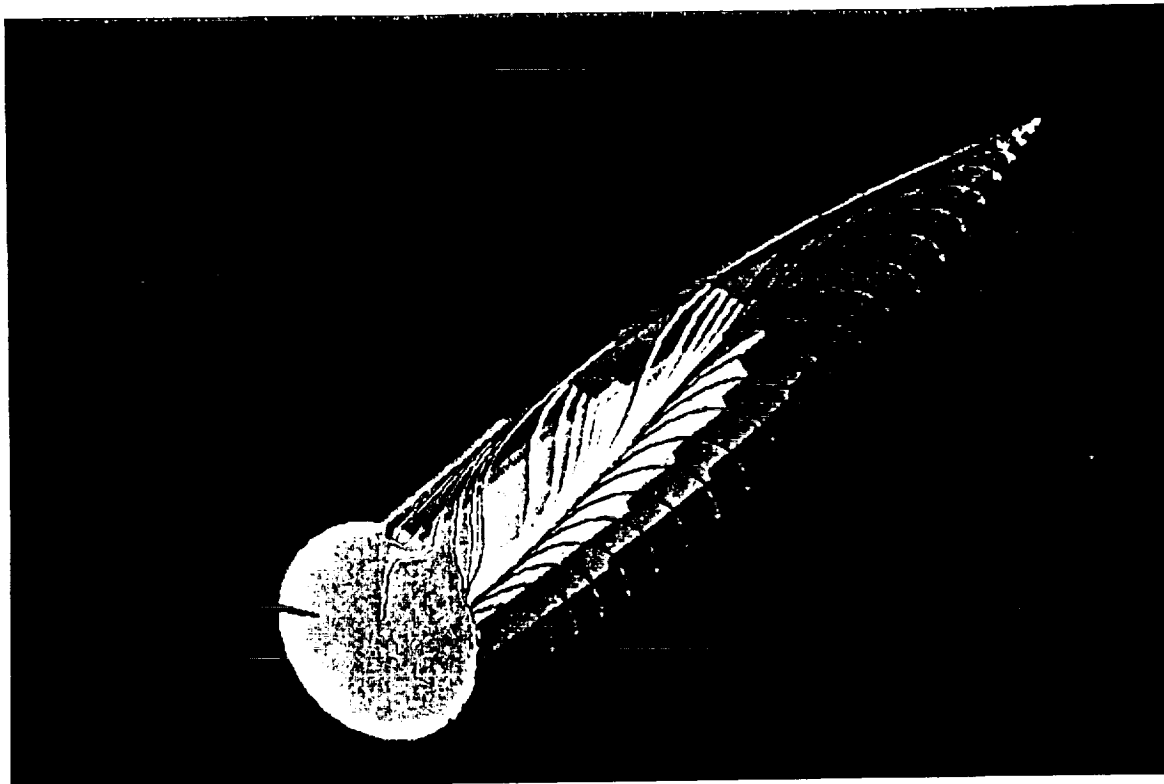


Figure 13.- Computed surface skin friction lines for $\alpha = 30^\circ$.

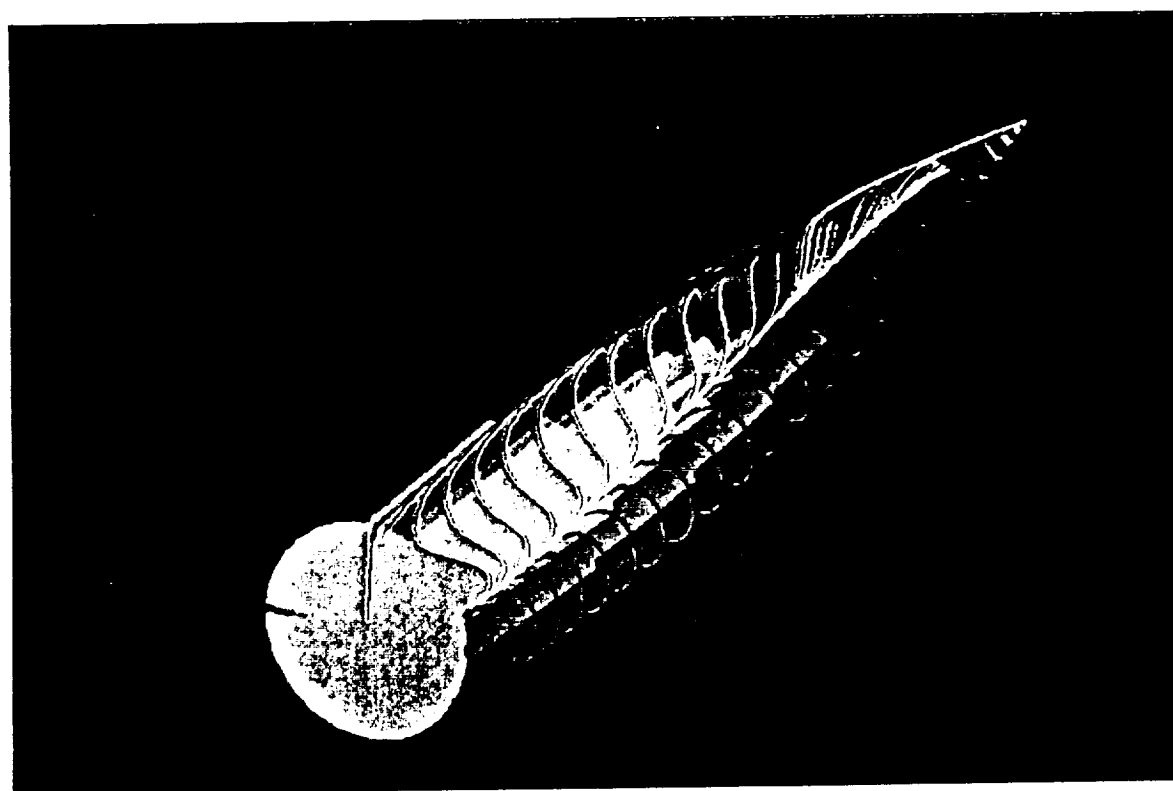


Figure 14.- Computed surface skin friction lines for $\alpha = 45^\circ$.

1. Report No. NASA TM-88329	2. Government Accession No.	3. Recipient's Catalog No.	
4. Title and Subtitle A COMPUTATIONAL/EXPERIMENTAL STUDY OF THE FLOW AROUND A BODY OF REVOLUTION AT ANGLE OF ATTACK		5. Report Date September 1986	
		6. Performing Organization Code	
7. Author(s) Gregory G. Zilliac		8. Performing Organization Report No. A-86319	
		10. Work Unit No.	
9. Performing Organization Name and Address Ames Research Center Moffett Field, CA 94035		11. Contract or Grant No.	
		13. Type of Report and Period Covered Technical Memorandum	
12. Sponsoring Agency Name and Address National Aeronautics and Space Administration Washington, DC 20546		14. Sponsoring Agency Code 505-60-31	
15. Supplementary Notes Point of Contact: Greg Zilliac, Ames Research Center, M/S 260-1 Moffett Field, CA 94035 (415) 694-4142 or FTS 464-4142			
16. Abstract The incompressible Navier-Stokes equations are numerically solved for steady flow around an ogive-cylinder (finess ratio 4.5) at angle of attack. The three-dimensional vortical flow is investigated with emphasis on the tip and the near wake region. The implicit, finite-difference computation is performed on the CRAY X-MP computer using the method of pseudo-compressibility. Comparisons of computational results with results of a companion towing tank experiment are presented for two symmetric leeside flow cases of moderate angles of attack. The topology of the flow is discussed and conclusions are drawn concerning the growth and stability of the primary vortices.			
17. Key Words (Suggested by Author(s)) Body of revolution 3-D Navier-Stokes solution High angle of attack Vortices		18. Distribution Statement Unlimited Subject Category - 34	
19. Security Classif. (of this report) Unclassified	20. Security Classif. (of this page) Unclassified	21. No. of Pages 35	22. Price* A02